Pacific Climate Futures training, Federated States of Micronesia

Chapter 6
Projections Based on Global Climate Models

Summary

- The climate change projections in this chapter are based on simulations from up to 18 global climate models for three emissions scenarios: B1 (low), A1B (medium) and A2 (high). Results are given for three future 20-year periods centred on 2030, 2055 and 2090, relative to a 20-year period centred on 1990.
- The projected warming over the PCCSP region is about 70% as large as the global average warming for all emissions scenarios. Regional warming is expected to be greatest near the equator. Large increases in the incidence of extremely hot days and warm nights are also projected.
- Increases in annual mean rainfall are projected to be most prominent near the South Pacific Convergence Zone (SPCZ) and Intertropical Convergence Zone (ITCZ), while the remainder of the region is generally expected to experience little change. Little change is projected in the annual number of rainy days, except for increases near the equator. A widespread increase in the number of heavy and extreme rain days is projected.
- Increases in potential evapotranspiration are expected. The ratio of annual average rainfall to potential evapotranspiration decreases in most regions (increased aridity), except near the equator where the relatively large projected rainfall increases exceed the smaller changes in potential evapotranspiration.
- Surface wind speed generally decreases in the equatorial and northern parts of the region, while increases are indicated in the south, but these changes are projected to be relatively small in most locations. Changes in wind direction are very small.
- Projected changes in humidity and solar radiation are also relatively small (less than 5% by 2090).
- Sea-surface salinity is expected to decrease in the West Pacific Warm Pool. The regional pattern of change closely matches projected changes in net rainfall (i.e. rainfall minus evaporation). The intensified warming and freshening at the surface is projected to make the surface ocean less dense compared to the deep ocean, so the ocean becomes more stratified.
- Sea level is projected to rise. However, improved understanding of the processes responsible for ice-sheet changes are urgently required to improve estimates of the rate and timing of 21st century and longer-term sea-level rise. For the PCCSP region, total sea-level rise is projected to be similar to the global average.
- The projected growth in atmospheric carbon dioxide concentration is expected to cause further ocean acidification leading to increasingly marginal conditions for sustaining healthy coral growth and reef ecosystems.
- The El Niño-Southern Oscillation (ENSO) will continue to be a major source of climate variability. However the impacts of global warming on ENSO amplitude and frequency are unclear.
- While broad-scale patterns of change are physically plausible and relatively consistent between models (at least in the vicinity of the ITCZ and SPCZ), the small-scale details of these projections should be interpreted with caution, given the deficiencies in model simulations of the current climate described in Chapter 5.

6.1 Introduction

The Intergovernmental Panel on Climate Change (IPCC) gives broad-scale projections for the Pacific (Mimura et al., 2007). Annual mean temperature and rainfall projections are averaged over two large Pacific regions (the North Pacific and the South Pacific), for three 30-year periods (2010–2039, 2040–2069 and 2070–2099), based on results from seven global climate models and four emissions scenarios. The projected warming is slightly greater in the north than the south, and rainfall tends to increase in the north with no clear direction of change in the south. An increase in the frequency of extremely high temperatures is likely, with more heavy rainfall and more intense cyclones, but the global total number of cyclones may decrease. Global average sea-level may rise 0.18 to 0.59 m by 2080–2099, relative to 1980–1999, but larger increases cannot be ruled out.

The level of regional detail in the IPCC projections is limited over the PCCSP region. In this chapter, more detail is provided. The climate change projections developed are based on simulations from up to 18 global climate models for three emissions scenarios (B1, A1B and A2, which are low, medium and high respectively).

Results are given for three future 20-year periods: 2020–2039 (denoted 2030), 2045–2064 (denoted 2055) and 2080–2099 (denoted 2090). Changes are relative to 1980–1999 (denoted 1990) (Figure 4.3). The selection of years and emissions scenarios is limited by data availability. The selection of models is based on those considered most reliable in Chapter 5 (Table 5.9).

The presentation of climate projections for the PCCSP region in this chapter focuses on multi-model mean changes (or multi-model median for variables with large outliers). While these may be considered to represent central estimates, this chapter also refers to the spread of individual model projections, relevant model biases and deficiencies (Chapter 5), the consistency of the projections with observed changes over recent decades (Chapter 3) and the physical plausibility of each projection. For a more detailed discussion on the full range of possible futures simulated for each country, see Volume 2.

6.2 Atmospheric Projections

Projected surface changes in air temperature, rainfall, wind, solar radiation, relative humidity and potential evapotranspiration are presented for the entire PCCSP region. More detailed atmospheric projections for the PCCSP region are available in Perkins et al. (in press), and for individual countries in Volume 2.

6.2.1 Surface Air Temperature

For all time periods, seasons, emissions scenarios and locations within the PCCSP region, mean air temperature (1.5 m above the ground) is projected to increase throughout the 21st century. The multi-model mean projections indicate a 0.5–1.0°C rise in annual mean temperature under all emissions scenarios by 2030, relative to the 1990 reference period (Figure 6.1). By 2055, the warming is generally 1.0–1.5°C with regional differences depending on the emissions scenario. By 2090, the warming is generally 1.5–2.0°C for B1 (low) emissions, around 2.0–2.5°C for A1B (medium) emissions, and around 2.5–3.0°C for A2 (high) emissions. This divergence of warming with time is consistent with the respective carbon dioxide (CO_2) concentration paths for each emissions scenario (Figure 4.1). Although not shown, seasonal projections (May-October; November-April) of surface air temperature are very similar to annual projections.

Despite the high level of model agreement in the direction and magnitude of temperature change (Perkins et al., in press), it should be noted that the models share common biases in the PCCSP region that directly influence the surface temperature projections. In particular, the largest warming occurs in the vicinity of Kiribati and Nauru, where the models are known to display a cold tongue bias with respect to their simulation of the current climate (Section 5.2.1.1 and Box 5.2). Temperature projections in this region may therefore be associated with a lower level of confidence than other locations (Volume 2).

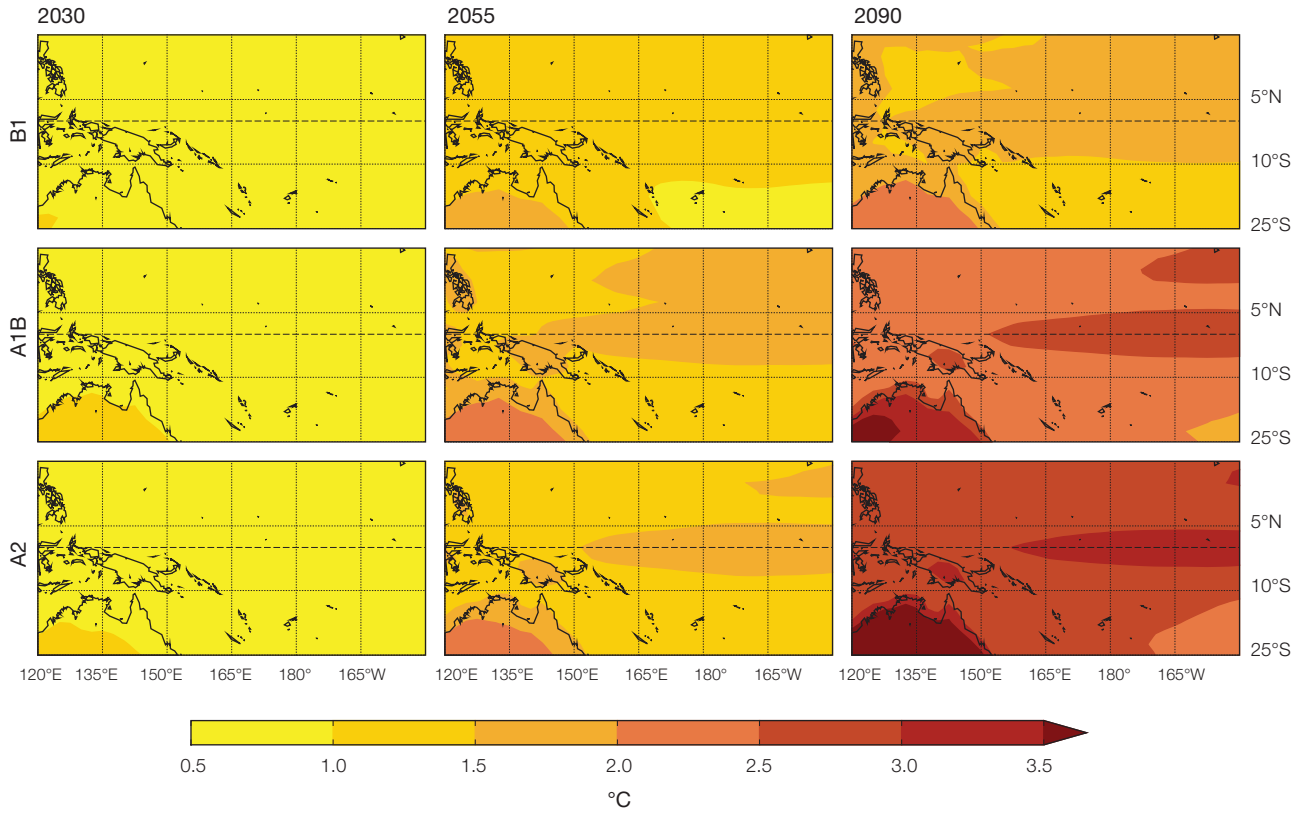

Figure 6.1: Projected multi-model mean changes in annual mean surface air temperature for 2030, 2055 and 2090, relative to 1990, under the B1 (low), A1B (medium) and A2 (high) emissions scenarios. All models agree on the direction of change in all locations.

The projected warming over the PCCSP region is less than the global average for all emissions scenarios, with the ratio between the PCCSP region and global change approximately constant at 0.7 throughout the 21st century (Figure 6.2). This phenomenon is linked to the fact that the global oceans have been warming (and are projected to warm into the future) at a lower rate than global land areas (c.f. Sections 3.2 and 6.3). As the PCCSP region has a higher percentage of ocean surface than the global average, it follows that temperature increases in the region would be less than those seen globally. The physical mechanism behind this land-sea contrast is not just a transient effect due to the larger heat capacity of the oceans, but an inherent feature of the climate system related to the different moisture availability over the land and ocean (Joshi et al., 2007; Dommenget, 2009).

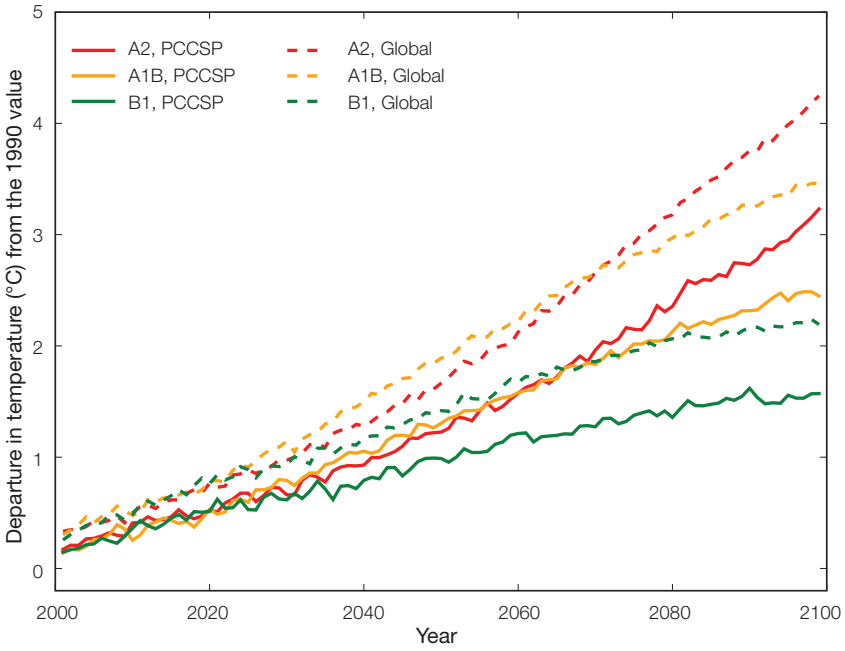

Figure 6.2: Projected multi-model mean changes in the spatial average global and PCCSP region annual mean surface air temperature for the 21st century, relative to 1990, under the B1 (low), A1B (medium) and A2 (high) emissions scenarios.

6.2.2 Rainfall

Wetter conditions are projected over most of the PCCSP region in the future (Figure 6.3). Strong increases in annual mean rainfall are projected in the vicinity of the Intertropical Convergence Zone (ITCZ) and South Pacific Convergence Zone (SPCZ), associated with increased moisture convergence in a warmer climate (Sections 6.4.3 and 6.4.5). In these regions, at least 80% of the models agree on an increase in rainfall. The largest increases are found immediately to the north of Papua New Guinea and the Solomon Islands.

The multi-model mean projections indicate increases in annual rainfall of 0–0.3 mm per day by 2030 throughout most of the PCCSP region, rising to 0.3–0.6 mm per day between latitudes 5°N and 10°S, for all emissions scenarios. By 2055, the increases are generally similar to 2030, but reach 0.9–1.2 mm per day between latitudes 5°N and 10°S, with decreases of 0–0.3 mm per day between Vanuatu and Tonga in the B1 (low) and A1B (medium) emissions scenarios. By 2090, the increases are generally similar to 2055, but reach 1.2–1.5 mm per day for B1 (low) emissions and 1.5–1.8 mm per day for A1B (medium) and A2 (high) emissions between latitudes 5°N and 10°S (Figure 6.3).

On a seasonal basis, rainfall increases are widespread during November-April and associated with an intensification of the SPCZ and West Pacific Monsoon (Figure 6.4; Sections 6.4.4 and 6.4.5). Rainfall increases are also projected during May-October in the deep tropics (Section 6.4.3), while decreases in rainfall are projected to the south of the SPCZ mean position, between Vanuatu and the Cook Islands.

While this broad-scale pattern of rainfall change is both physically plausible and relatively consistent between models (at least in the deep tropics and in the vicinity of the SPCZ), the small-scale details of these projections should be interpreted with caution, given known biases in model simulations of the current climate. In particular, the orientation of the SPCZ tends to be overly zonal (east-west) in most simulations (Section 5.2.3.3), while the seasonal migration of the ITCZ tends to be overestimated during the Northern Hemisphere summer (Section 5.2.3.4). The models also substantially underestimate current rainfall in the vicinity of Kiribati and Nauru, in association with the cold tongue bias (Section 5.2.1.2).

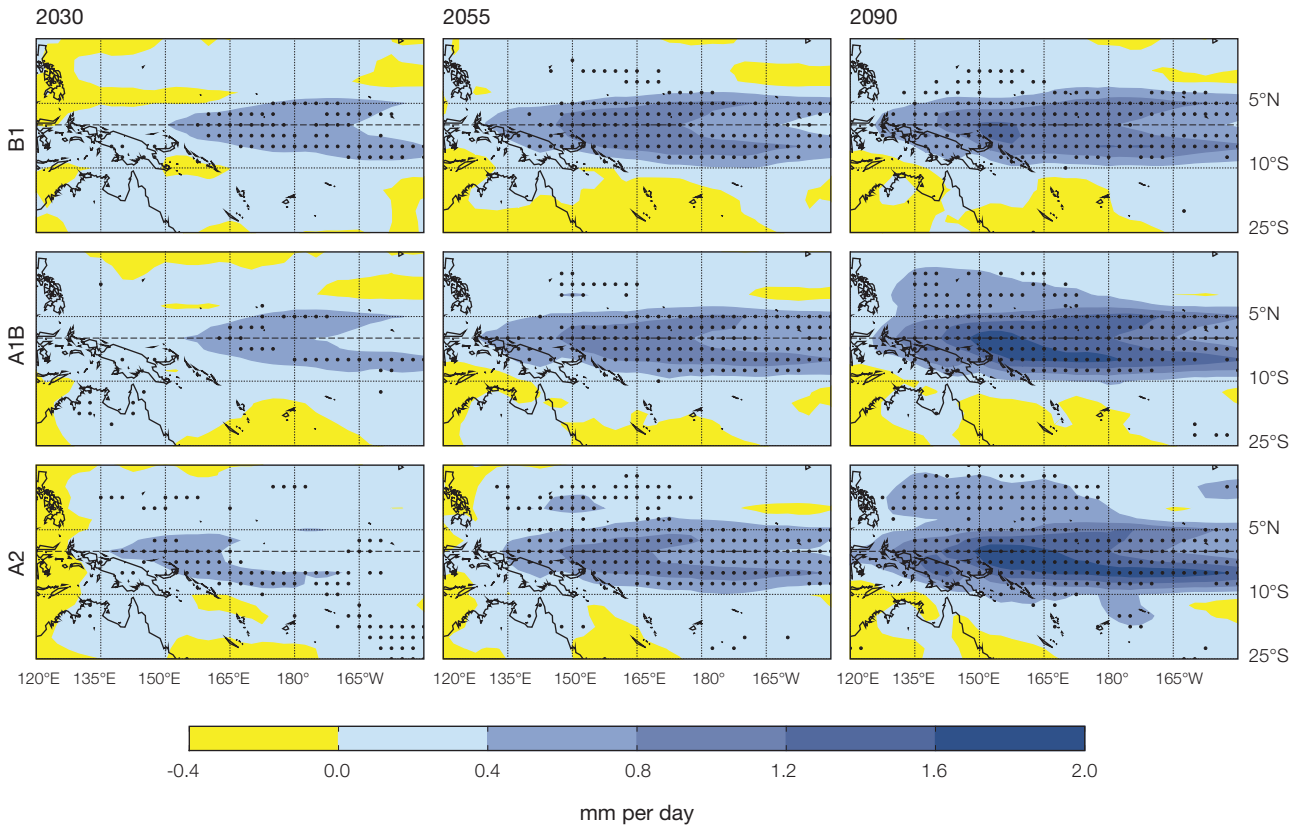

Figure 6.3: Projected multi-model mean changes in annual rainfall (mm per day) for 2030, 2055 and 2090, relative to 1990, under the B1 (low), A1B (medium) and A2 (high) emissions scenarios. Regions where at least 80% of models agree on the direction of change are stippled.

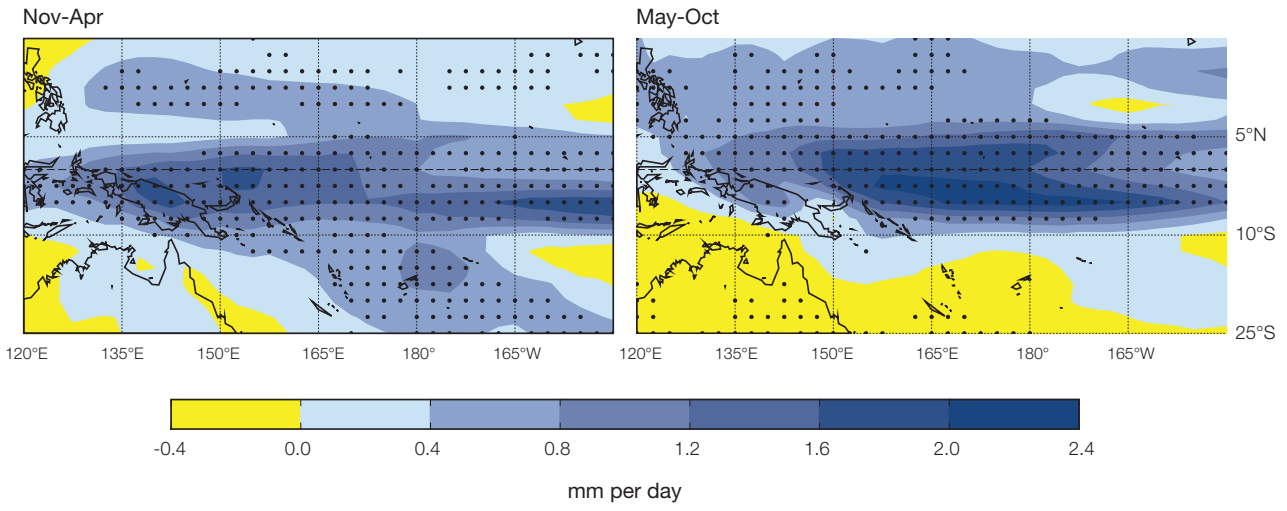

Figure 6.4: Projected multi-model mean changes in November-April (left) and May-October (right) mean rainfall for 2090, relative to 1990, under the A2 (high) emissions scenario. Regions where at least 80% of models agree on the direction of change are stippled.

6.2.3 Near-Surface Wind

Near-surface wind speed (10 m above the ground) is generally projected to decrease in the equatorial and northern parts of the PCCSP region, while increases are projected in the south (Figure 6.5). However, the multi-model annual and seasonal median changes are relatively small in most locations, with values of typically less than ±0.5 metres per second (± ~10%) projected for all emissions scenarios and time periods. Wind speed in the vicinity of the Cook Islands is an exception, where the May-October mean wind speed is projected to increase by up to 1.5 metres per second (~40%) in 2090 under the A2 (high) scenario.

From a physical standpoint, these wind speed increases in the south-east of the PCCSP region have been linked to the relatively low rate of sea-surface temperature increase in that region (Xie et al., 2010), while the wind speed decline projected for the equatorial PCCSP region is consistent with a weakening of the Walker Circulation (Vecchi and Soden, 2007b; Power and Kociuba, in press). The models tend to closely agree with observed annual mean wind speed data throughout most of the PCCSP region, so the projections are considered robust. However, the models tend to overestimate the annual mean wind speed immediately to the north and east of Papua New Guinea and the Solomon Islands, so projections are considered less reliable there (Section 5.2.1.3).

Projected multi-model median changes in annual and seasonal wind direction are typically less than 3° throughout much of the PCCSP region, for all emissions scenarios and time periods. As such, no large-scale, fundamental shift in the near-surface circulation is indicated.

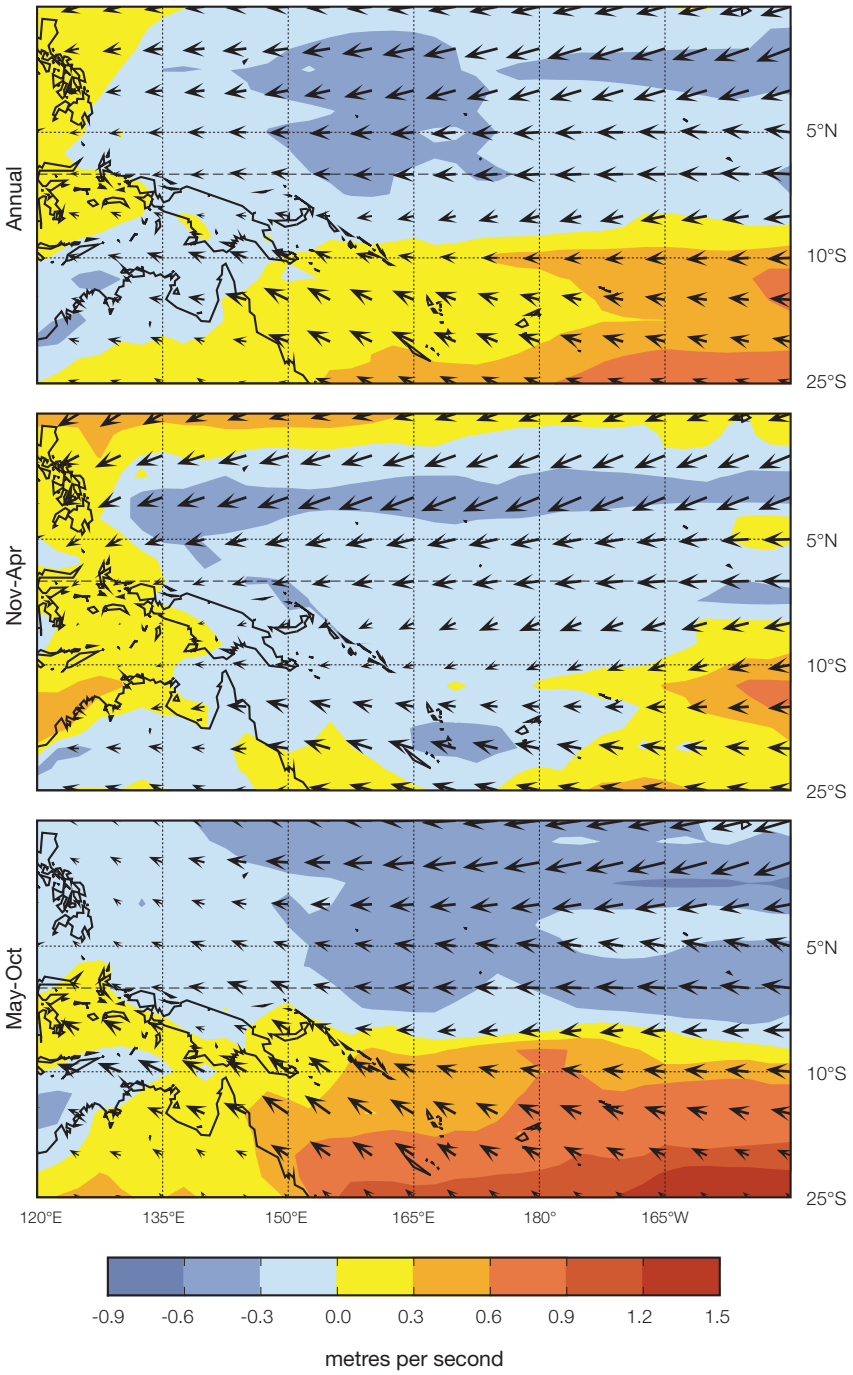

Figure 6.5: Projected multi-model median change in annual and seasonal mean wind speed (metres per second) for 2090, relative to 1990, under the A2 (high) emissions scenario. For reference, the multi-model median 1990 annual mean wind field is indicated by arrows. Projected changes for 2030 and 2055 and lower emission scenarios tend to be of smaller magnitude but similar spatial structure.

6.2.4 Surface Solar Radiation

Given the strong link between changes in cloud cover and surface solar radiation, projected multi-model mean changes in annual surface solar radiation closely resemble those for rainfall. For instance, the projected decline in surface solar radiation in the deep tropics (latitudes 10°S to 5°N) and in the vicinity of the SPCZ (Figure 6.6) is consistent with the projected increase in rainfall in these areas (through an associated increase in cloudiness; Figures 6.3 and 6.4). In fact, multi-model mean decreases in annual surface solar radiation of up to -14 Watts per square metre (~5%) are projected for 2090 under the A2 (high) scenario, in the region immediately to the north of Papua New Guinea and the Solomon Islands. For locations not influenced by the SPCZ or ITCZ, projected decreases in surface solar radiation are relatively small, with individual model projections tending to cluster relatively close to and either side of no change. As for rainfall, small-scale details in projected surface solar radiation need to be interpreted with caution, due to known biases in model simulations of the ITCZ and SPCZ (Sections 5.2.3.3 and 5.2.3.4), in addition to the cold tongue bias (Section 5.2.1.1).

6.2.5 Near-Surface Humidity

Relative humidity is defined as the amount of water vapour in the air, relative to the maximum amount of water vapour that the air is able to hold, without it condensing (expressed as a percentage). Projected changes in near-surface relative humidity (1.5 m above the ground) tend to be small, with spatial multi-model mean values ranging from changes of between -0.5 to +0.5% in 2030 for the B1 (low) scenario, to -0.5 to +1.5% in 2090 for the A2 (high) scenario (Figure 6.7).

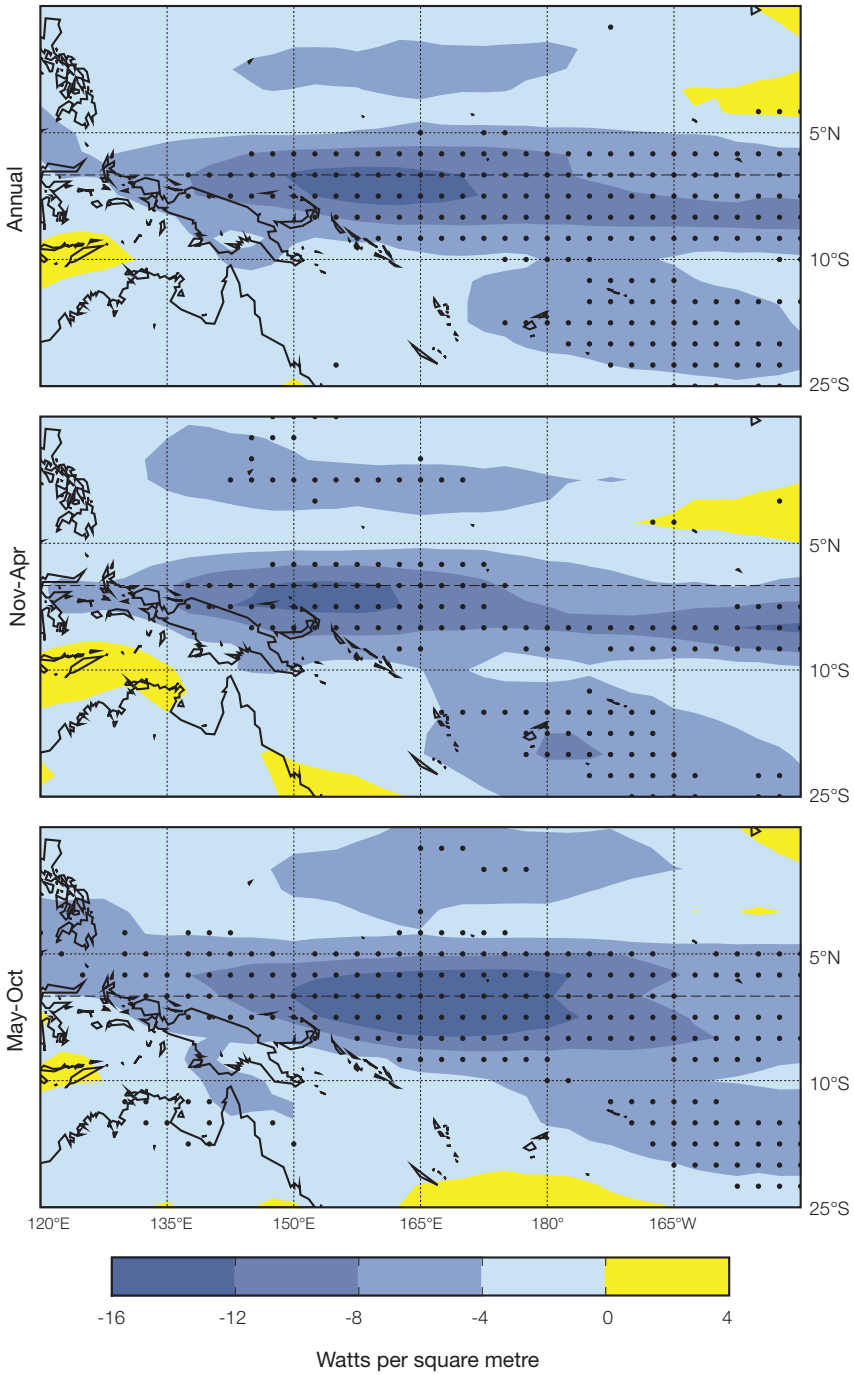

Figure 6.6: Projected multi-model mean changes in annual and seasonal mean surface solar radiation (Watts per square metre) for 2090, relative to 1990, under the A2 (high) emissions scenario. Projected changes for earlier years and less intense emissions scenarios tend to be of smaller magnitude but similar spatial structure. Regions where at least 80% of models agree on the direction of change are stippled.

Although small in magnitude, these projections consistently indicate declining relative humidity in locations associated with large land masses, such as Papua New Guinea and East Timor. This is likely due to the fact that there is a limited supply of water over vast expanses of land, meaning the actual amount of water vapour in the air cannot increase at the same rate as the water vapour holding capacity of the atmosphere (which increases as temperature increases). Due to the essentially unlimited supply of water for evaporation from the vast expanses of ocean, decreases in relative humidity of similar magnitude are not seen elsewhere throughout the PCCSP region. A physical reason for regional contrasts that are not related to water availability, such as the presence of relatively high projected changes in the south of the PCCSP region, is an area of ongoing research (Sherwood et al., 2010).

6.2.6 Potential Evapotranspiration

Evapotranspiration is the sum of evaporation from the land surface (e.g. from the soil and bodies of water such as lakes and rivers) and transpiration from vegetation. Potential evapotranspiration is therefore defined as the evapotranspiration that would take place if there was an unlimited water supply (Morton, 1983). It is a representation of the environmental demand for evapotranspiration, which depends upon both the amount of energy available to evaporate water, and the strength of the wind available to transport water vapour from the surface up into the lower atmosphere. Potential evapotranspiration is therefore highest in hot, sunny (high surface solar radiation), dry (low relative humidity), and windy conditions.

Throughout much of the PCCSP region, annual mean potential evapotranspiration is projected to increase into the future (Figure 6.8). The spatial consistency of this finding suggests that the projected increase in annual mean temperature (which promotes an increase in potential evapotranspiration) dominates the future evolution of potential evapotranspiration, overwhelming the influence of changes in other related variables, such as solar radiation. An exception to this general rule is evident for a small region extending from immediately north of Papua New Guinea and the Solomon Islands eastwards beyond Nauru and Tuvalu, where approximately half of the CMIP3 models project a decrease in potential evapotranspiration.

It is useful to consider these projected changes to the environmental demand for evapotranspiration in the context of future rainfall changes. In particular, projected changes in the ratio of annual average rainfall and potential evapotranspiration (known as the aridity index; Middleton and Thomas, 1992) can be used to infer long-term changes in the balance between these two important hydrological parameters. Throughout much of the PCCSP region, a slight decrease in the aridity index is projected into the future, indicating that the projected increase in environmental demand for moisture is not being matched by sufficient increases in rainfall (i.e. the environment becomes slightly more arid; Figure 6.8). In the vicinity of Kiribati, Nauru and Tuvalu however, the relatively large projected rainfall increases overwhelm the smaller changes in potential evapotranspiration, meaning that the aridity index is projected to increase (these regions are projected to become less arid).

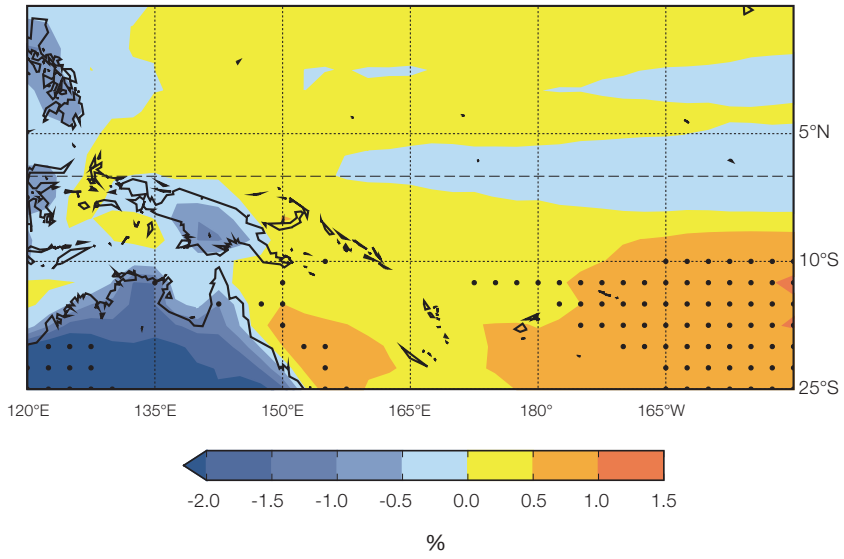

Figure 6.7: Projected multi-model mean change (%) in annual relative humidity for 2090, relative to 1990, for the A2 (high) emissions scenario. Projected changes for earlier years and less intense emissions scenarios tend to be of smaller magnitude but similar spatial structure. Regions where at least 80% of models agree on the direction of change are stippled.

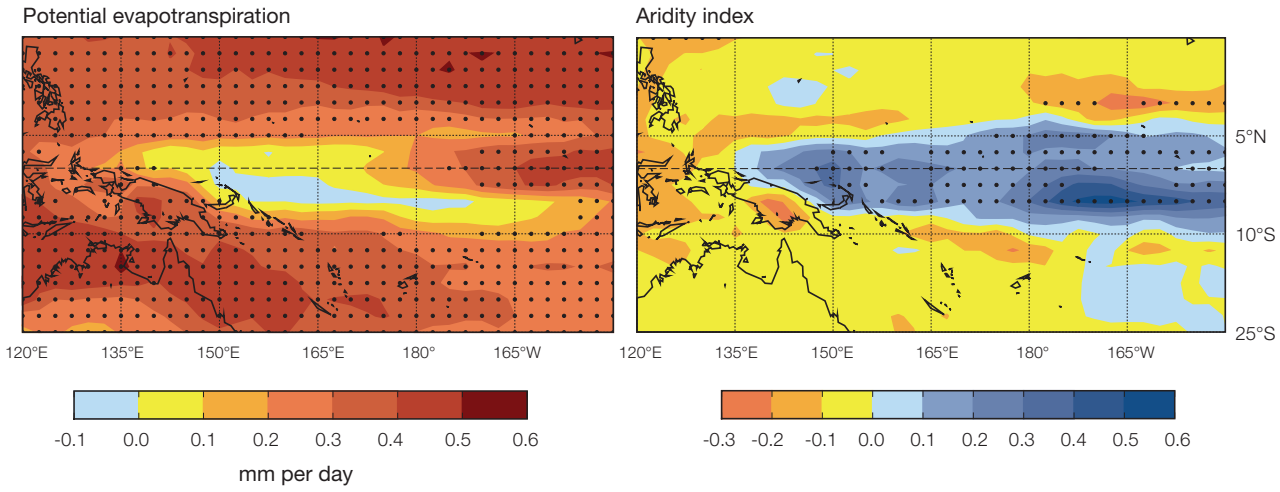

Figure 6.8: Projected multi-model median change in annual mean potential evapotranspiration (mm per day) and aridity index, (rainfall/potential evaporation), for 2090, relative to 1990, for the A2 (high) emissions scenario. Note that a negative change in the aridity index indicates a shift towards a more arid environment. Projected changes for earlier years and less intense emissions scenarios tend to be of smaller magnitude but similar spatial structure. Regions where at least 80% of models agree on the direction of change are stippled.

6.2.7 Extreme Temperature and Rainfall

Changes in the mean climate are almost inevitably associated with changes in the frequency and intensity of extreme events. For instance, a rise in mean temperature may be associated with an increase (decrease) in the number of extremely hot (cold) days, while a rise in mean rainfall may be associated with an increase in the number of heavy rain days, at the expense of light rain days (Figure 6.9). However, due to the inherent complexity of the climate system, changes in extremes are not always consistent with changes in the mean, so it is generally not appropriate to simply extrapolate mean climate projections when considering extreme events. Instead, a number of descriptive indices (Frich et al., 2002; Alexander et al., 2006; Klein Tank et al., 2009) and statistical modelling techniques (Coles et al., 2001; Kharin et al., 2005; Kharin et al., 2007) are used to capture changes in the magnitude and frequency of extreme weather events from daily data.

In this section, daily CMIP3 data have been analysed to provide projected changes in a number of commonly used extreme maximum temperature, minimum temperature and rainfall indices (Table 6.1), as well as a drought index. Since the availability of daily CMIP3 data is less than that for monthly data, both in terms of the number of contributing models (Appendix 1, Table A2) and the future time periods offered, projections are presented for two 20-year periods centred on 2055 and 2090. For those projections where the changes are relatively uniform and of the same direction across the PCCSP region, the regional average multi-model mean change (plus or minus twice the inter-model standard deviation) is provided only for 2090 under the A2 (high) scenario.

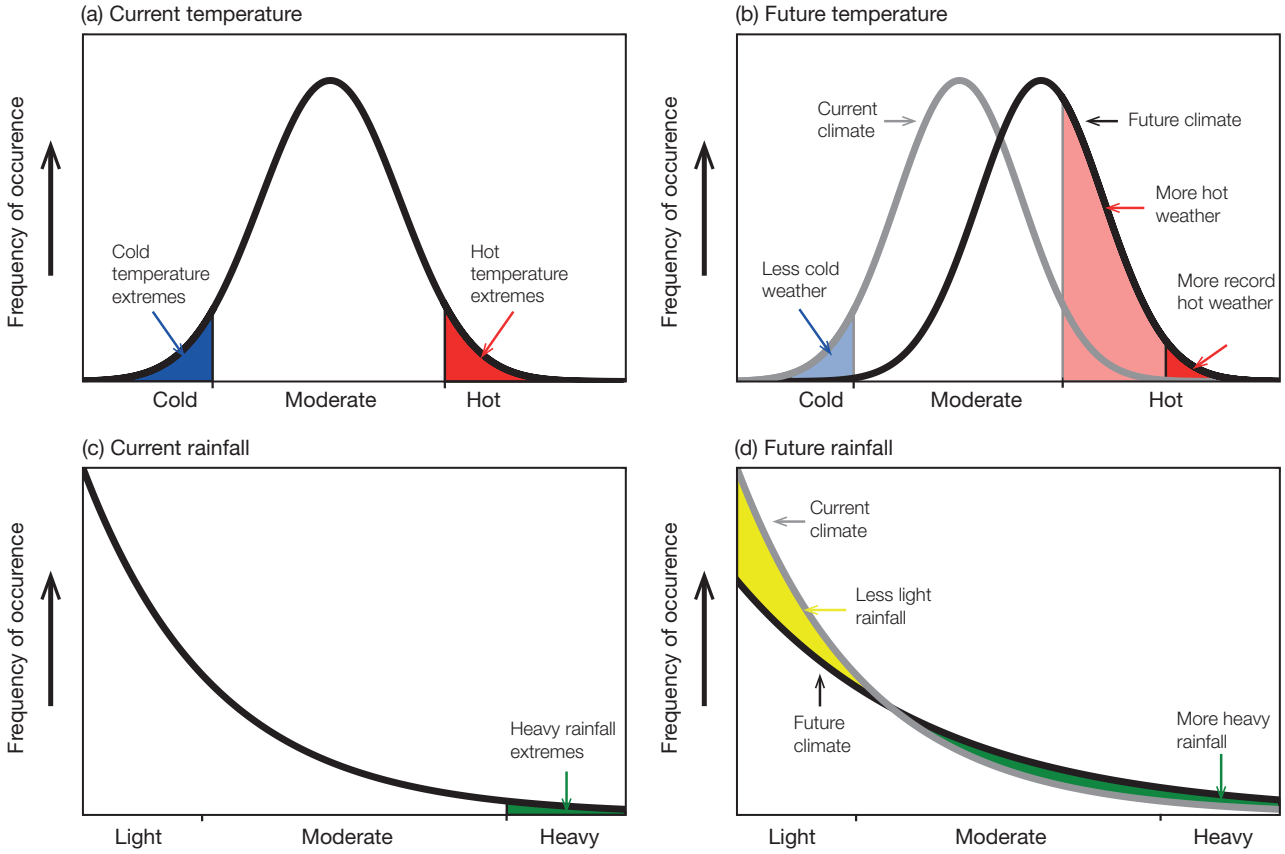

Figure 6.9: Typical changes to the occurrence of extreme events in response to a hypothetical increase in mean temperature and rainfall. Panels (a) and (c) represent the current climate and demonstrate averages and extremes for temperature and rainfall, respectively. Panels (b) and (d) show the changes in extreme events arising from an increase in mean temperature and rainfall, respectively. Adapted from figure ES.1 of the US Climate Change Science Program, Karl et al., (2009).

Table 6.1: Statistics used to project changes in the magnitude and frequency of extreme events.

Statistic	Description	Variables
1-in-20-year return value [a]	Extreme daily value that occurs on average only once every 20 years The change in this statistic relative to the base period (1980–1999) is denoted ΔP_{20RV}	Maximum temperature Minimum temperature Rainfall
90th percentile	The value that is only exceeded on 10% of days	Maximum temperature Minimum temperature Rainfall
10th percentile	The value that is surpassed on all but 10% of days	Maximum temperature Minimum temperature Rainfall
Highest 5-day total rainfall [b]	Magnitude of the highest 5-day rainfall total The change in this statistic relative to the base period (1980–1999) is denoted ΔP_{RX5}	Rainfall
Extreme rainfall contribution index [b]	Percentage of total annual rainfall that comes from intense rainfall events (defined as more intense than the 99th percentile) The change in this statistic relative to the base period (1980–1999) is denoted $\Delta P_{R99pTOT}$	Rainfall
Rainy day	Any day where more than 1 mm of rain falls	Rainfall
Light, moderate and heavy rain day[c]	Any day where 1–10 mm (light), 10–20 mm (moderate) or 20–50 mm (heavy) of rain falls	Rainfall

[a] Calculated using the Generalised Extreme Value distribution (Coles et al., 2001; Kharin et al., 2005)
[b] See http://cccma.seos.uvic.ca/ETCCDMI/ for details
[c] Categories defined by Dai (2006) and Sun et al. (2006).

6.2.7.1 Surface Air Temperature Extremes

Projected changes in surface air temperature extremes, both in terms of their magnitude and spatial structure, are highly consistent with mean temperature projections presented in Section 6.2.1. The projected multi-model mean increase in the annual 10th percentile, 90th percentile and 1-in-20-year minimum and maximum daily temperature all range from 0.5 to 1.5°C for 2055 under the B1 (low) scenario, to 2.0 to 3.5°C for 2090 under the A2 (high) scenario. As such, it appears that the daily temperature distribution is projected to shift to warmer values, with little change to the range (or spread) of values. This differs from projections for many other regions of the globe, where minimum temperatures are projected to increase at a faster rate than maximum temperatures, indicating a change in the spread of the distribution as well as the location (Meehl et al., 2007b; Kharin et al., 2007).

The spatial distribution of changes in extreme surface air temperature is comparable to that of mean surface air temperature. For example, under the A2 (high) emissions scenario by 2055, the 1-in-20-year maximum daily temperature event increases by up to 2°C over Papua New Guinea, and in the central and north-east of the PCCSP region; and by 2090 the area with the smallest increase of 2.5°C is situated in the south-west of the region, with increases of up to 3°C projected for the majority of the region (Figure 6.10). Such patterns and magnitudes are also projected for near-surface air temperature (Figure 6.1), however there are some regional differences, most notably that the warming in the central equatorial part of the region is 0.5°C less in the maximum 1-in-20-year event than for mean surface air temperature (Figures 6.10 and 6.1, respectively).

Over all locations, the current 1-in-20-year maximum daily temperature event is projected to increase in frequency. Given the relatively narrow range of daily temperatures that many (particularly near-equatorial) PCCSP Partner Countries experience, the projected increases in frequency are significantly larger than what is expected over land based regions (Kharin et al., 2007). Due to the shift of the overall temperature distribution towards warmer conditions, there are no projected occurrences of the current 1-in-20-year daily minimum temperature in 2030 and beyond.

The uncertainty associated with extreme temperature projections is higher than for mean temperature projections. This is due to a larger spread in the model projections around the multi-model mean value (Perkins, in press), in addition to the fact that the CMIP3 models tend to underestimate the magnitude of temperature extremes in the current climate (Section 5.2.4.1).

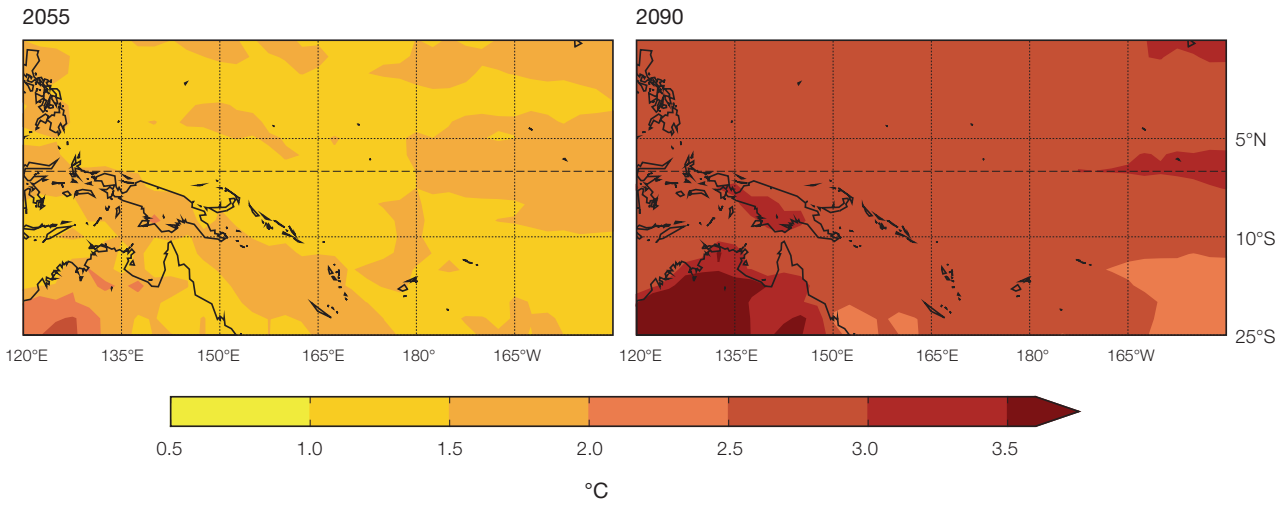

Figure 6.10: Projected multi-model mean changes in the 1-in-20-year maximum daily surface air temperature (°C) for 2055 and 2090, relative to 1990, under the A2 (high) emissions scenario. All models agree on the direction of change in all locations.

6.2.7.2 Extreme Daily Rainfall

A widespread increase in the number of heavy rain days (20–50 mm) is projected by the climate models for the A2 (high) emissions scenario. The annual numbers of rain days (over 1 mm), light rain days (1–10 mm) and moderate rain days (10–20 mm) are projected to increase near the equator, with little change elsewhere in the region (Figure 6.11).

For the A2 (high) scenario, this shift towards a rainfall distribution that includes more heavy rain days is projected to be accompanied by an increase in the intensity of extreme events (ΔP_{20RV} = 25 ± 70 mm or 35 ± 90%). Consequently, the maximum five-day rainfall total is also projected to increase in all locations (ΔP_{RX5} = 55 ± 200 mm or 30 ± 95%), and for most locations a greater percentage of annual rainfall is projected to come from intense rainfall events ($\Delta P_{R99pTOT}$ = 5 ± 10%). Extreme rainfall events that currently occur once every 20 years on average are simulated to occur four times per year, on average, by 2055 and seven times per year, on average, by 2090 under the A2 (high) scenario. It is clear that these projected increases in extreme rainfall are more pronounced than for the mean rainfall projections (Section 6.2.2).

Due to the large spread in projections between the CMIP3 climate models, and to the fact that all models tend to underestimate the current intensity and frequency of extreme rainfall events (Section 5.2.4.2), these projections must be interpreted with caution.

6.2.7.3 Drought

The standardised precipitation index (SPI; Lloyd-Hughes and Saunders, 2002) is a measure of drought based solely on rainfall (excluding the effect of evapotranspiration). It is computed by fitting a probability density function to the frequency distribution of rainfall which is summed over the timescale of interest (Lloyd-Hughes and Saunders, 2002). In this case, monthly precipitation is used and the timescale of interest is 12 months, chosen to reflect the time required for water deficit conditions to significantly affect various agricultural and hydrological systems. Each monthly value is the total precipitation for the previous 12 months. The probability distribution is then transformed to a standardised normal distribution. Negative SPI values are indicative of drought conditions while positive values are

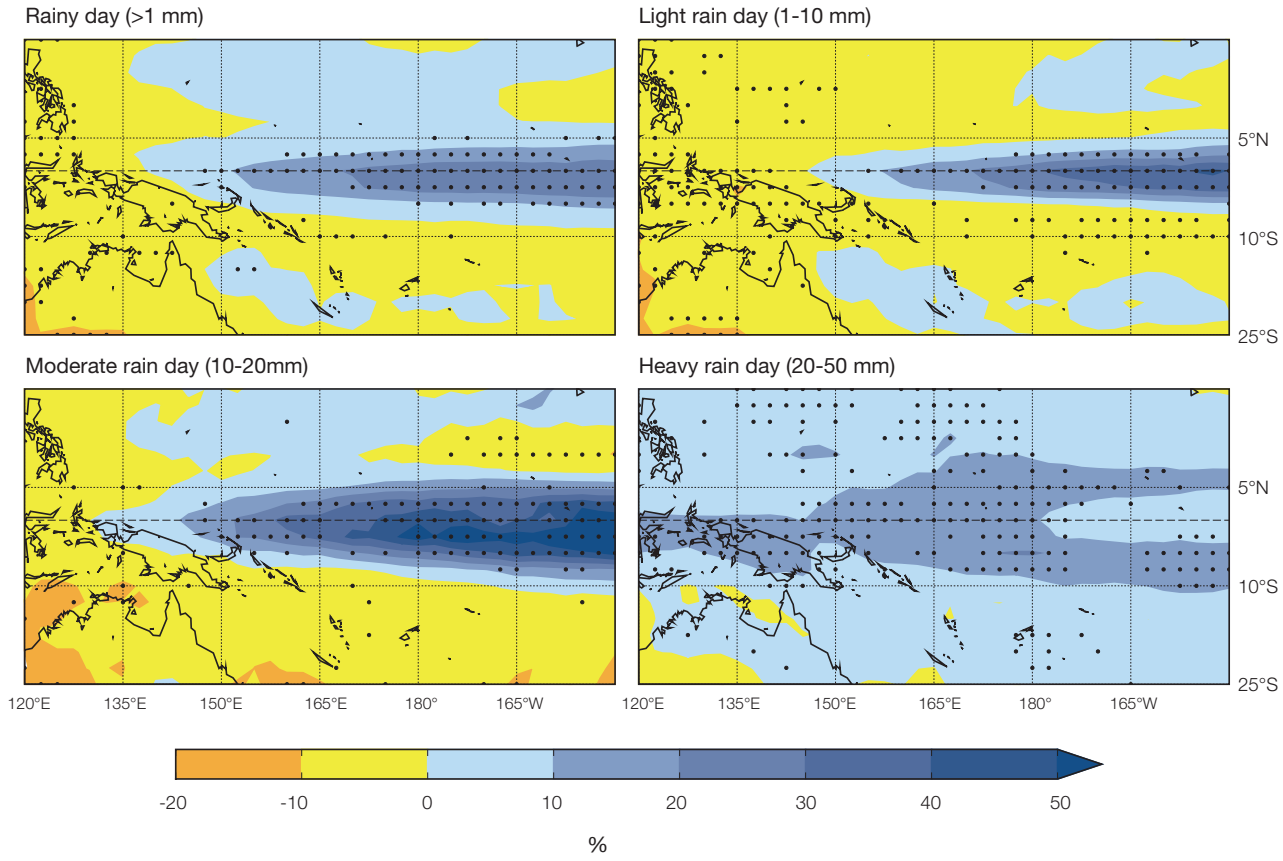

Figure 6.11: Projected multi-model mean change in the number of rainy (>1 mm), light rain (1–10 mm), moderate rain (10–20 mm) and heavy rain (20–50 mm) days between 1990 and 2090, for the A2 (high) emissions scenario. Regions where at least 80% of models agree on the direction of change are stippled.

indicative of water surplus conditions. Over the 21st century, the SPI for a given region has a mean of zero, due to normalisation. In general, there is a trend from negative to positive SPI values (i.e. fewer droughts toward the end of the century).

For all emissions scenarios, the frequency of moderate droughts (SPI values between -2.00 and -2.99) are projected to decline in the central Pacific (Figure 6.12). Over the eastern equatorial cold tongue region (Section 5.2.1.1), moderate droughts occur 3-4 times every 20 years by 2030, decreasing to 2-3 times by 2090. Over the central western Pacific (including Papua New Guinea, the Solomon Islands and southern Palau), moderate droughts occur 1-2 times every 20 years by 2030, decreasing to 0-1 times by 2090, particularly under the A2 (high) scenario. For the rest of the PCCSP region, the occurrence of moderate droughts remains as 1-2 times every 20 years, with the exception of a decrease in the north (over the Marshall Islands and Federated States of Micronesia) under the A2 (high) scenario.

Similar patterns are also evident for mild droughts (SPI values between -1.00 to -1.99) and severe droughts (SPI values between -3.00 to -3.99). Mild droughts decrease in the central Pacific from 9 times every 20 years by 2030 to 4-6 times every 20 years by 2090. Severe droughts decrease from 1-2 times every 20 years by 2030 to 0-1 times every 20 years by 2090. The largest decrease is simulated under the A2 (high) scenario, where the increase in rainfall is the highest (Figure 6.3). Regional projections of drought frequency are discussed for each country in Volume 2.

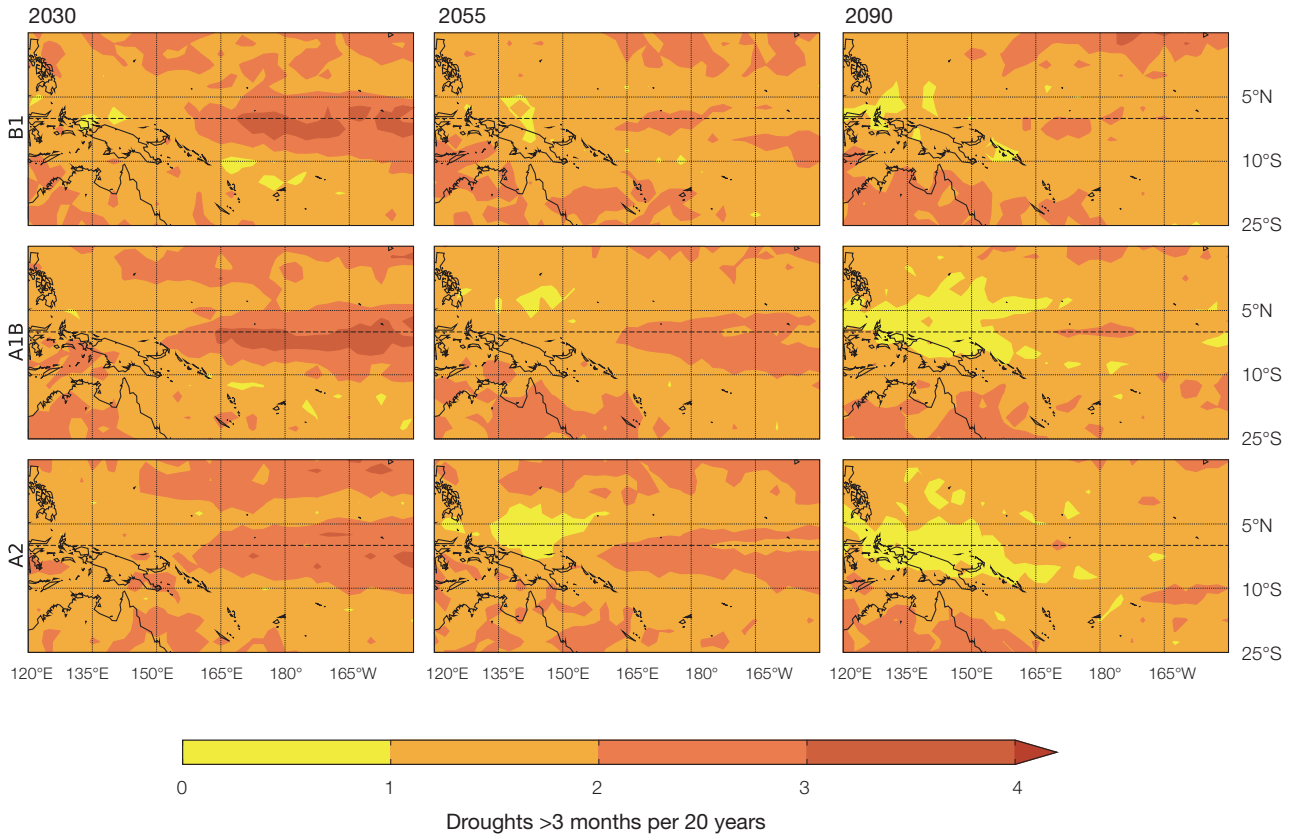

Figure 6.12: Frequency of moderate drought defined by the standardised precipitation index (SPI) under the B1 (low), A1B (medium) and A2 (high) scenarios for 20-year periods centred on 2030, 2055 and 2090. Frequency is defined as the number of times during the 20-year period where the SPI is between -2.00 to -2.99 for at least three consecutive months (Lloyd-Hughes and Saunders, 2002).

6.3 Ocean Projections

This section considers sea-surface temperature, sea-surface salinity, stratification and ocean circulation. Sea-level rise is addressed in Section 6.5 and ocean acidification is covered in Section 6.6.

Projections have been derived for three 20-year periods centred on 2030, 2055 and 2090, relative to a 20-year period centred on 1990. This is based on all available CMIP3 climate models, except those deemed unsatisfactory in their ability to simulate the aspects of the current climate (Chapter 5). The number of available models differs between each variable and emissions scenario (Appendix 1, Table A3).

6.3.1 Ocean Temperature and Salinity

Warming and freshening in the western tropical Pacific Ocean have already been observed over recent decades (Section 3.6; Cravatte, 2009).

In addition, climate models have consistently shown such changes for the 20th century and project acceleration into the future under the influence of human-induced global warming. For the PCCSP region, sea-surface temperatures are projected to increase by 1.4 ± 0.7°C, 2.2 ± 0.8°C and 2.6 ± 0.6°C and sea-surface salinities are projected to decrease by 0.22 ± 0.3 psu, 0.32 ± 0.4 psu and 0.34 ± 0.4 psu between 1990 and 2090 for the B1 (low), A1B (medium) and A2 (high) scenarios respectively (Figure 6.13), where the range is estimated as a two standard deviation spread over climate model projections. Differences in the rate of sea-surface temperatures rise between the A1B and A2 scenarios only emerge at the very end of the century because it is then that CO_2 concentrations for the A2 scenario start to overtake A1B (Figure 4.1). For the first few decades of the 21st century, CO_2 concentrations for A1B slightly exceed those of A2.

The spread in future sea-surface salinity changes across the models is considerably larger than for sea-surface temperature, reflecting in part large inter-model differences in the representation of mean rainfall.

Many of the climate models indicate a maximum warming in the central equatorial Pacific, with the least warming occurring in the south-eastern Pacific (Figure 6.14). The pattern of equatorial warming has been shown to be related to a complicated set of factors, including greater cloud cover in combination with weaker westward surface flow in the eastern Pacific, and weaker upwelling of sub-surface water combined with a stronger vertical temperature gradient in the western Pacific (DiNezio et al., 2009). The weak warming in the south-eastern Pacific may be linked to the stronger projected winds in that region that will tend to cool the ocean (Xie et al., 2009).

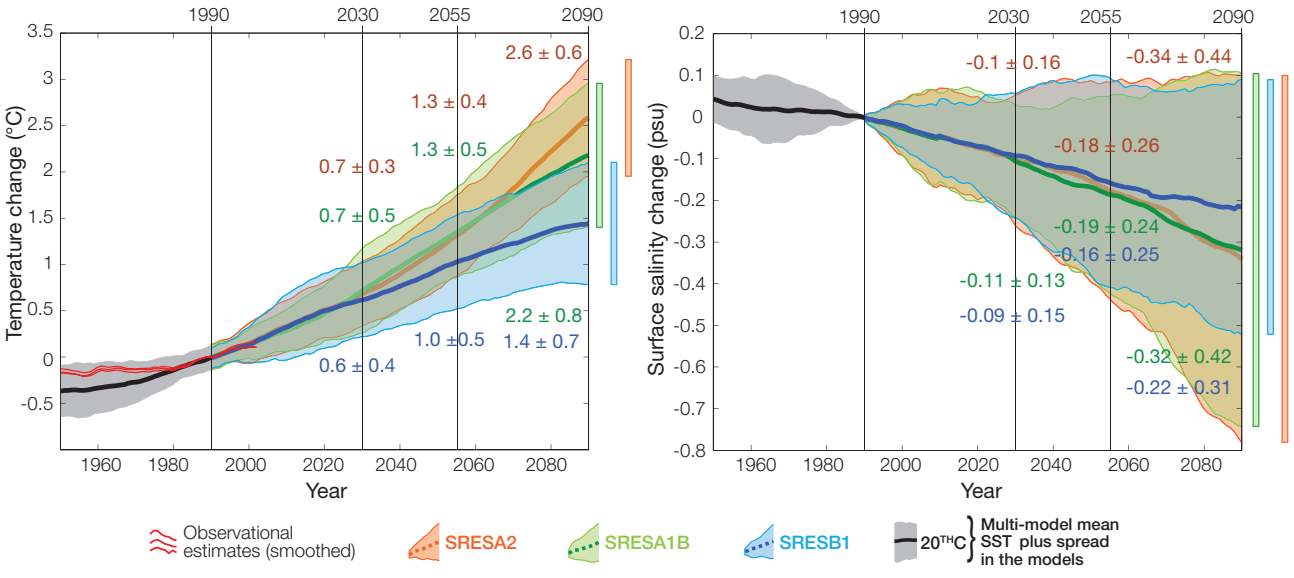

Figure 6.13: Evolution of multi-model average sea-surface temperatures (°C) (left) and sea surface salinity (psu) (right) for the PCCSP region for 1950–1990 (black) and three post-1990 scenarios (B1-green, A1B-blue and A2-red). The shaded envelope indicates ± two standard deviations. Numbers indicate mean change in sea-surface temperature or salinity (plus or minus the corresponding multi-model standard deviation) for three time slices (2030, 2055 and 2090) relative to 1990. The red line (left) is observational estimate from HadISST. Where possible de-drifting has involved the removal of any linear trend in the control simulation for 1900–2150. While the ECHAM5/MPI-OM model has no sea-surface temperature control run available for de-drifting, the equivalent control run for surface air temperature shows relatively minor drift, and the model has been included in this analysis.

Regional differences in projected salinity changes (Figure 6.14) closely match projected changes in net rainfall (i.e. rainfall minus evaporation). The largest increases in rainfall occur in the western equatorial Pacific, and on the inner flanks of the convergence zones, with reduced rainfall in the south-east. This results in a strong freshening in most of the PCCSP region (with high agreement between models), except in the far eastern and particularly south-eastern parts of the domain, where there is a suggestion of increased salinity.

The West Pacific Warm Pool provides the energy to sustain western Pacific convection and the tropical atmospheric circulation. It is an important factor in El Niño-Southern Oscillation (ENSO) variability; it can modulate the intensification of tropical cyclones, and its eastern edge is an important indicator of the location of vital tuna stocks on inter annual time scales (Lehodey et al., 1997). The projected changes for the West Pacific Warm Pool show a massive increase in extent (defined here as temperatures above 29˚C), with the edge of the pool moving many thousands of kilometres to the east along the equator over coming decades (Figure 6.14). While the fresh water pool also shows a substantial increase in area, the changes are considerably less than the Warm Pool. This indicates that the threshold sea-surface temperature for convective activity must also be increasing over time so that the area of strongest convection does not expand with the 29˚C isotherm (see also Johnson and Xie, 2010 and references therein).

The projected changes in temperature and salinity with depth, averaged over the PCCSP region (Figure 6.15), show that the surface intensified warming and freshening will cause the surface ocean to become considerably less dense compared to the deep ocean, i.e. the ocean becomes more stratified (with 100% model agreement). There is also a clear projected increase in ocean stratification (as measured by the buoyancy frequency squared, which depends on the vertical density gradient) between about 50 m and 100 m depth. These depths are associated with the upper pycnocline, which marks the boundary between high nutrients (below) and depleted nutrients (above) (Chapter 2). This increase in stratification acts to inhibit mixing, thereby reducing the supply of nutrients from the deep to the surface ocean, with consequences for biological productivity (Ganachaud et al., 2011). Implications of the projected changes for ocean biology, particularly fisheries, are discussed in detail in Bell et al. (2011).

6.3.2 Ocean Circulation

Theoretical arguments for a surface warming and an intensification of the hydrological cycle also suggest that the tropical atmospheric circulation, including the equatorial trade winds, should weaken (Held and Soden, 2006) as the troposphere warms. Observational evidence indicates that such a slowdown may have already occurred (Vecchi et al., 2006; Power and Smith, 2007; Power and Kociuba, 2010, in press). Climate models do indeed project a consistent slowdown of the equatorial trade winds with a weakening of surface winds over much of the Northern Hemisphere extra-tropics and a corresponding strengthening in the Southern Hemisphere. Surface Ekman currents (wind driven flow that is deflected by the Earth's rotation) in the upper few tens of metres of the ocean, are directly driven by surface winds. The direction of flow is complicated by the rotation of the planet, causing surface currents to be deflected to the right (left) of the direction of the wind in the Northern (Southern) Hemisphere. No deflection occurs at the equator (where the Coriolis effect vanishes). Thus in

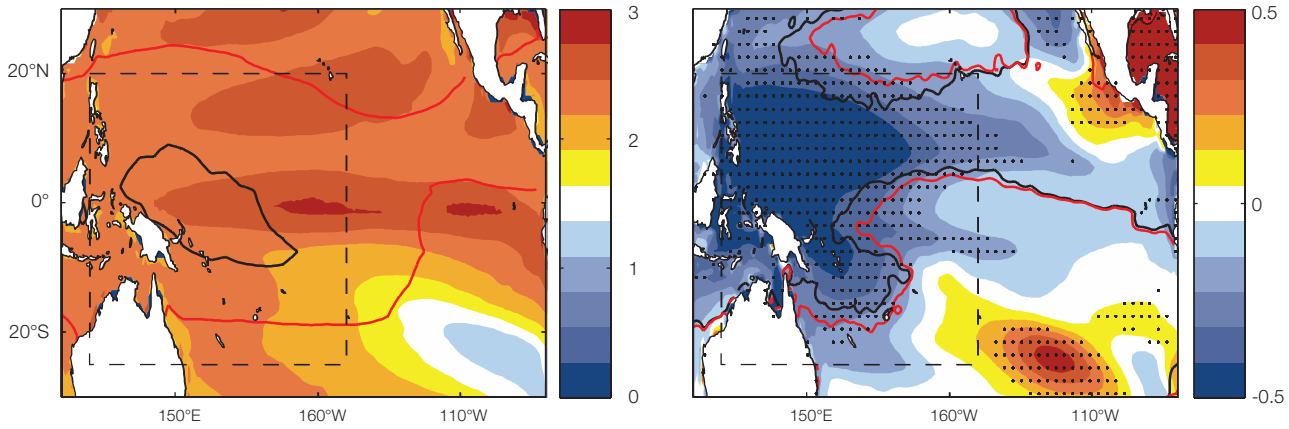

Figure 6.14: Multi-model mean change in sea-surface temperature (°C) (left) and sea-surface salinity (psu) (right) over the tropical Pacific region for the A2 (high) scenario, for a 20-year period centred on 2090 relative to 1990. Superimposed on the sea-surface temperature change is the observed (HadISST) Warm Pool extent (black contour, for waters with mean annual temperature exceeding 29°C) and projected Warm Pool extent (red contour, computed as 1990 observed sea-surface temperature + projected warming). Superimposed on sea-surface salinity change is the observed (black, from CARS06) and projected (red) location of the edge of the 'fresh pool' defined by the 34.8 psu contour. Stippling for sea-surface salinity represents areas where there is at least 80% agreement in the sign of the change across the models. Drift correction has been applied to all models.

regions of projected decreases in surface wind strength, surface currents will also tend to weaken. Just to the north and south of the equator, the mean equatorial trade winds drive a mean surface Ekman current with a component directed away from the equator. This divergent surface flow normally generates upwelling along the equator, with an associated convergent surface flow and downwelling off the equator, driving a shallow vertical circulation (the tropical overturning cell). The projected slow-down of the equatorial trade winds drives a weakening of the surface Ekman flow and consequently a slowdown of the tropical overturning cell.

Model projections show the changes in the volume transport (measured in millions of cubic metres per second; Sv) for some of the major regional currents (Figure 6.16). There is a robust acceleration of the northern branch of the sub-tropical gyre, which forms the extra-tropical part of the South Equatorial Current. This change is part of a large-scale intensification of the sub-tropical gyre including the East Australian Current (Cai and Cowan, 2007; Sen Gupta et al., 2009). Conversely, the part of the South Equatorial Current close to the equator weakens as a direct response to the weakening trade winds. While there is a projected weakening in the multi-model mean, there exists poor agreement across the models. Similarly, circulation changes in the Northern Hemisphere are not very consistent across the models. In a number of models there are projected increases in the sub-surface Equatorial Undercurrent, in part related to greater flow in the New Guinea Coastal Undercurrent which feeds the Equatorial Undercurrent. Finally, the Indonesian Throughflow, which represents the only conduit for tropical water to pass from the Pacific to the Indian Ocean, shows a robust decrease in water transport, from about 9 Sv to 7 Sv in the multi-model mean.

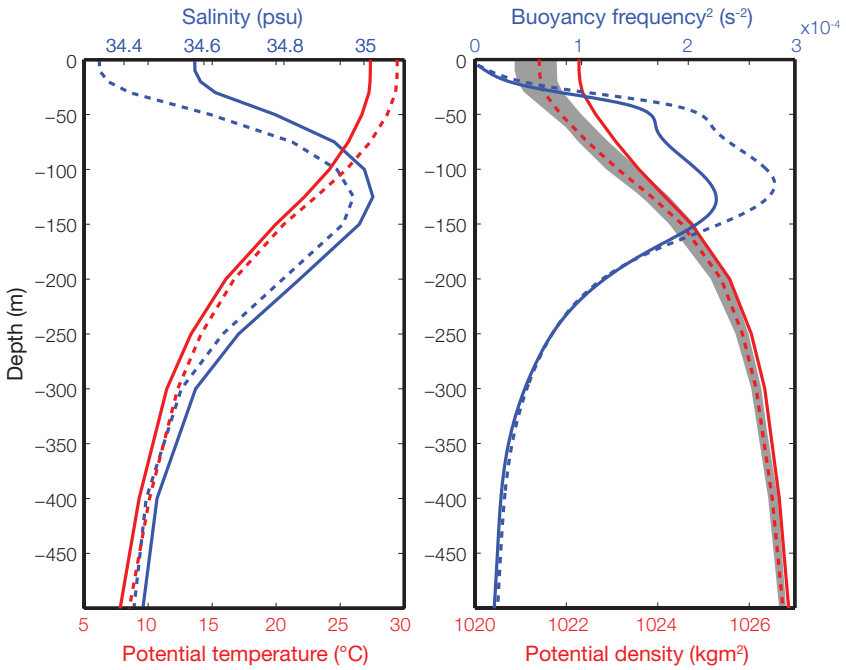

Figure 6.15: Ocean changes with depth. (Left) PCCSP regional average multi-model mean potential temperature (red) and salinity (blue), for the period 1980–1999 (solid) and 2080–2099 (dashed) for A1B scenario. (Right) PCCSP regional average multi-model mean potential density (red) and buoyancy frequency squared (blue), for 1980–1999 (solid) and 2080–2099 (dashed) for A1B (medium) scenario. Grey shading indicates the full range of projected density changes based on all models used (Chapter 4, Table A3). The buoyancy frequency N is defined as $(N^2 = \frac{1}{\rho}\frac{\partial \rho}{\partial z}$, where ρ is density and z is depth).

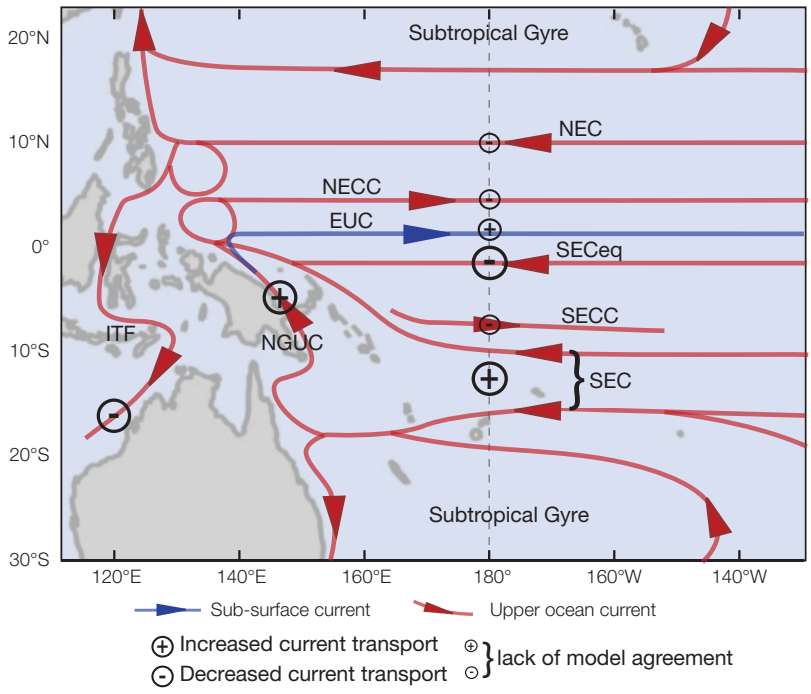

Figure 6.16: Schematic showing some of the major upper ocean currents and whether they are projected to increase or decrease in the future. Key: Equatorial Undercurrent (EUC); Indonesian Throughflow (ITF); North Equatorial Current (NEC); North Equatorial Counter Current (NECC); New Guinea Coastal Undercurrent (NGUC); South Equatorial Current (SEC); South Equatorial Counter Current (SECC).

6.4 Key Climate Features and Variability

6.4.1 El Niño-Southern Oscillation

ENSO events are responsible for significant climate variability in most Partner Countries. Even small changes to various aspects of ENSO could profoundly alter Pacific climate: the frequency and/or intensity of El Niño and La Niña events, and the details of their characteristics, such as where the strongest El Niño-related increase in sea-surface temperature occurs.

Projected changes in the average climate of the Pacific relevant to ENSO (Sections 6.2 and 6.3) are: increasing sea-surface and near-surface air temperatures, with the strongest warming on the equator; a flattening and shallowing of the thermocline (Yeh et al., 2009); an increase in ocean stratification; and a weakening of the Walker Circulation, with a decrease in the pressure gradient across the tropical Pacific (Vecchi et al., 2006; Power and Smith, 2007; Power and Kociuba, 2010, in press). As they are related to positive or negative feedbacks, some of these changes favour an intensification of ENSO variability and some favour a weakening. As a result, the exact nature of ENSO under conditions of global warming has many uncertainties (Collins et al., 2010).

The strength of the Niño3.4 and ENSO Modoki Indices for the CMIP3 climate model simulations for the 2078–2098 period using the A2 (high) scenario, relative to 1979–1999 in the 20th century simulations (Figure 6.17) shows that changes in the two indices are closely related across the different models. This suggests that sea-surface temperature variability changes in each model are fairly consistent across a broad equatorial Pacific region. All the models indicate that ENSO will remain an important factor in year-to-year variability in the future. However, studies of palaeoclimate suggest that ENSO has exhibited very different behaviours in past climates (Chapter 3).

Global warming has very likely driven changes in mean rainfall, temperature and other important climatic variables (Hegerl et al., 2007; Meehl et al., 2007b) in many countries (including PCCSP Partner Countries). As ENSO events are responsible for some of the variability about these means in most Partner Countries, climatic conditions experienced during ENSO events will very likely change if they have not already (Power and Smith, 2007). For example, if El Niño tends to warm a particular region then temperatures experienced during future El Niño events will tend to be higher than the temperatures experienced during past El Niño events.

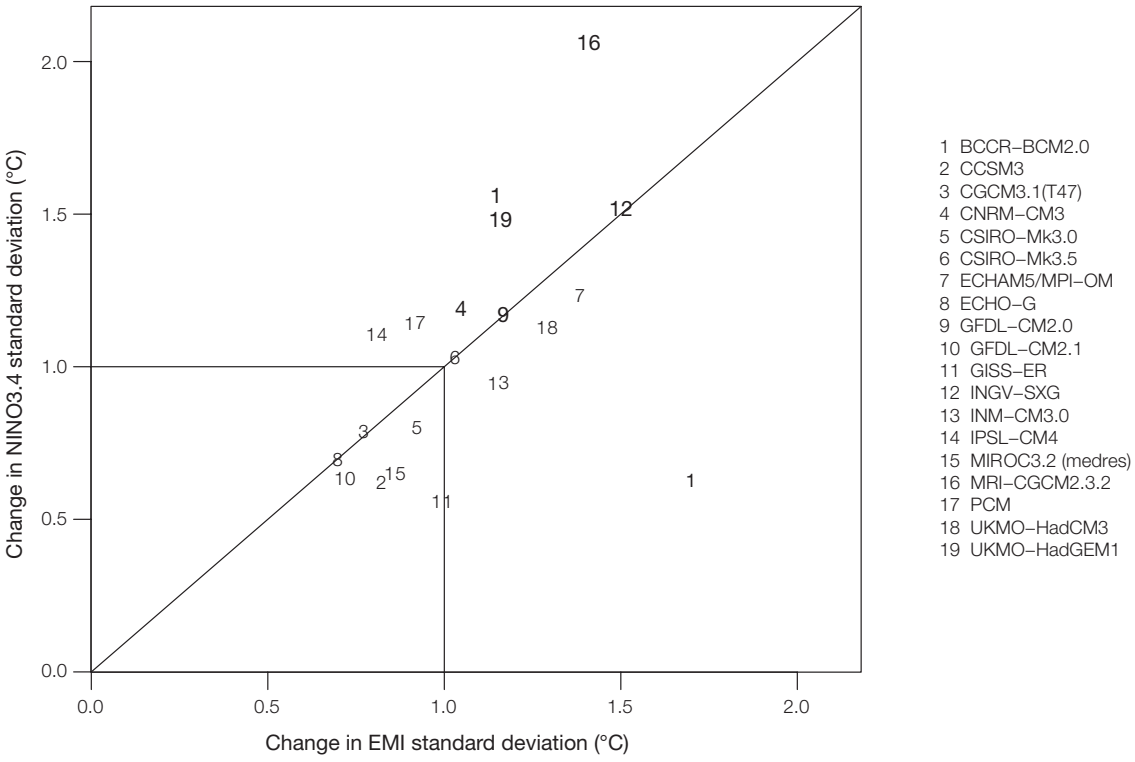

Figure 6.17: The ratio of A2 (high) scenario (2078–2098) to 20th century (1979–1999) model simulated variability (standard deviations) in the Niño3.4 and ENSO Modoki Indices (EMI) for 19 climate models. Numbers greater than one show increased variability in the future, while those less than one show decreased variability. The GISS-ER, INGV-SXG, INM-CM3.0 and PCM models are considered less reliable than the others (see Chapter 5).

It should be noted that any changes in ENSO variability, as seen in these projections, may be due to interdecadal variability in the strength of events, rather than any global warming signal. In the period 2057–2077, the relative changes in the two ENSO indices are slightly different for each model, but the range across all models is similar to that for 2078–2098. For some of the CMIP3 models, the changes in variability in the two periods are in opposite directions, but in the majority only the size of the changes are different, suggesting that some of the projected change is due to decadal variability, with the remainder due to global warming.

The models are generally poor in reproducing the pattern of sea-surface temperature variability associated with ENSO Modoki in the 20th century, and so little can be ascertained on the probable evolution of the Modoki under the A2 (high) scenario. However, this analysis (based on the Modoki index calculated across three boxes – see Section 3.4.1) shows no large, or consistent, change across the CMIP3 simulations.

The sea-surface temperature pattern across the Pacific region associated with the Interdecadal Pacific Oscillation (IPO) shares some features of the pattern of warming observed over the 20th century (Meehl et al., 2009). This means that in coming decades, depending on the phase of the IPO, natural interdecadal temperature variability may act to either enhance or reduce the warming driven by continued increases in greenhouse gas concentrations in locations where the IPO influences sea-surface temperatures. This same variability may also act over the next few decades to favour more El Niño or more La Niña type conditions. However, over longer time periods the global warming signal will dominate temperatures in the region.

Also, given the lack of evidence that ENSO variability will change significantly, over longer periods neither El Niño nor La Niña events would be expected to be significantly more prevalent than the other.

Therefore, while year-to-year variability in the PCCSP region will continue to be largely driven by ENSO, climate models do not provide consistent projections of changes in the frequency, intensity and patterns of future El Niño and La Niña events.

6.4.2 Indian Ocean Dipole

The frequency of positive Indian Ocean Dipole (IOD) events has been increasing in recent decades (Section 3.4.7). Climate models suggest that a more positive IOD-like mean-state will continue with easterly wind trends and a shallowing thermocline over the eastern Indian Ocean, associated with a weakening of the Walker Circulation (Vecchi and Soden, 2007b). A multi-model average shows a slower warming rate in the eastern Indian Ocean than in the western Indian Ocean (Cai et al., 2011), with a consistent rainfall response by way of lower rainfall over the eastern Indian Ocean regions, including East Timor (Figures 6.3 and 6.4).

However, there is no systematic multi-model analysis of how the IOD frequency and amplitude will change. It is anticipated that a more positive IOD-like mean state would be associated with an increase in the positive IOD amplitude and/or frequency. For example, a study using the GFDL model showed that there is little change in the positive IOD amplitude (Zheng et al., 2010), although the frequency of positive IOD events increases. Further research is required to assess the degree of consensus amongst models regarding projected changes in IOD frequency and amplitude.

6.4.3 Intertropical Convergence Zone

Under conditions of anthropogenically induced climate change, the multi-model mean projections using 16 CMIP3 models show a general increase in tropical rainfall, with increases occurring in a broad band (rather than confined to the ITCZ) extending fairly uniformly and zonally from around 10°S to 5°N across the Pacific (Figure 6.3). This pattern can be largely attributed to increased moisture convergence associated with warmer air temperatures (Christensen et al., 2007), although additional dynamics-related changes complicate the picture regionally in individual models (Chou et al., 2008). Changes in rainfall, averaged over the region north of the equator encompassing the ITCZ (160°E–120°W, 0–15°N), show a general increase in June-August (high levels of model consensus), with little change in December-February, thereby amplifying the current seasonal cycle (Figure 6.18a). Using the 6 mm per day contour to define the ITCZ, there is an increase in the area of the ITCZ in all models in June-August, and in all but three in December-February (Moise and Delage, in press). This corresponds to a modest expansion of around 5% per °C of Pacific warming, primarily through an increase in the width of the ITCZ. A 25–30% increase in annual mean rainfall is simulated by the end of the century within the ITCZ under the A2 (high) scenario.

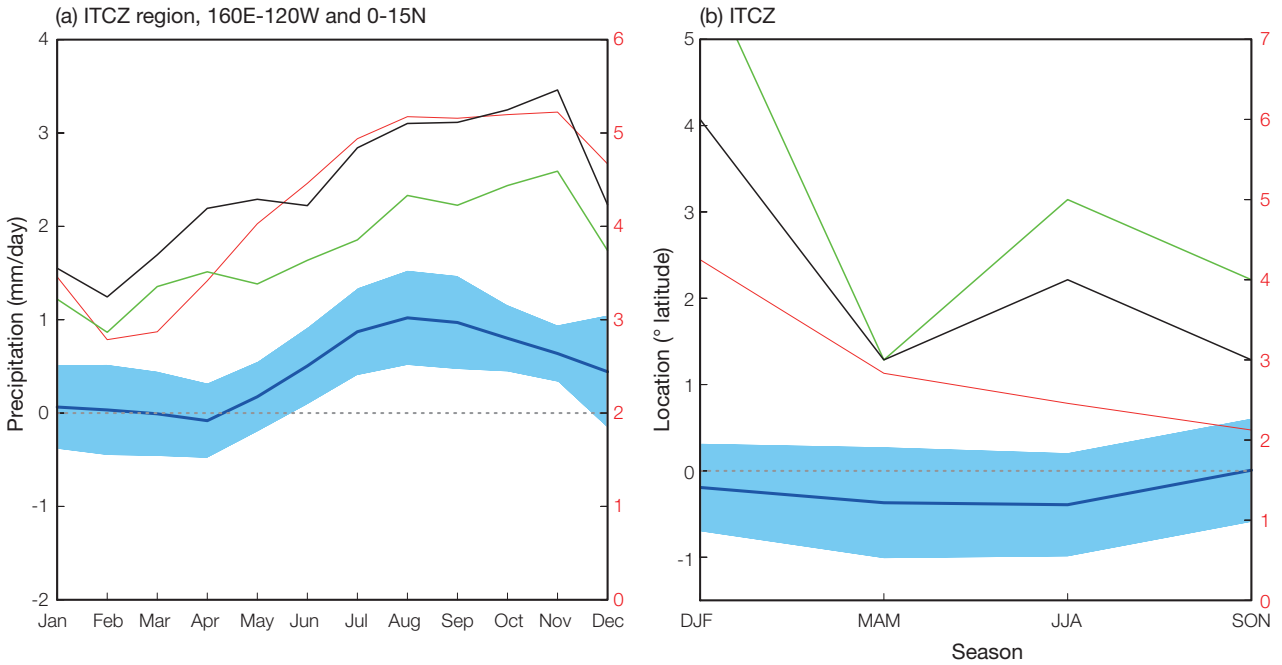

Figure 6.18: (a) Projected changes in average monthly rainfall (mm per day; relating to the left y-axis scale) over the ITCZ region (defined by 160°E–120°W, 0–15°N). The multi-model mean is shown as the thick blue line, with the shaded regions encompassing the spread (standard deviation) between individual model simulations. Also shown is the mean model 20th century annual cycle of monthly rainfall in red (mm per day; relating to the right y-axis scale) and observations from the GPCP (green) and CMAP (black) datasets respectively. (b) Projected changes in location (latitude; relating to the left y-axis scale) of the ITCZ. Also shown is the mean model and observed 20th century location of ITCZ (latitude; relating to the right y-axis scale). Line colours correspond to those in (a). Climate change results in both (a) and (b) show 2079–2098 A2 (high) emissions minus 1980–1999. Included are all models providing A2 (high) scenario results, except those listed in Table 5.9 as performing poorly.

Given the broad areal extent of the tropical rainfall increases exhibited by the CMIP3 models, only relatively small systematic geographical shifts are projected for the ITCZ location. Results using a line fitting method (Brown et al., 2011) between the longitudes 160°E and 120°W, show that the maximum shifts in particular models in individual seasons are modest, at less than 2° of latitude (Figure 6.18b), with the east-west orientation ('slope') of the ITCZ having little systematic change on average (not shown). In the multi-model mean, models show a small displacement (less than 0.5°) towards the equator in March-May and June-August (small compared with a mean location at 8°N), with a spread (standard deviation) much larger than the projected displacement, highlighting the significant degree of disagreement in these projections. For December-February and September-November, there is no change apparent in mean ITCZ location. This result is not sensitive to whether all CMIP3 models are used, or when those which show lower skill are excluded.

In summary, under the A2 (high) scenario, the ITCZ is projected to move equatorward in some seasons and broaden, but only by a very small amount (less than 2° of latitude), with substantial disagreement between individual models on the magnitude of the shift. A more robust projection is for significant rainfall increases, but these occur both in the ITCZ itself and in the surrounding (particularly equatorial) region.

6.4.4 West Pacific Monsoon

The West Pacific Monsoon region is rarely discussed exclusively in climate change scientific literature and the following discussion is based on results covering larger regions that either include or directly affect the West Pacific Monsoon. Under global warming, the Walker Circulation affects South Asian monsoon variability in such a way that the role of the Pacific Ocean dominates, and that of the Indian Ocean is secondary (Meehl and Arblaster, 2003). Climate projections show an increase in rainfall during the Asian monsoon, along with an increase in the interannual season-averaged variability. However, the uncertain role of aerosols in general, and carbon aerosols in particular, complicates

the monsoon rainfall projections (Meehl et al., 2007b). This region is also affected by the cold tongue bias present in all global climate models (Section 5.2.3.5).

There is no significant projected change in the westerly winds over the region, even though the results differ across individual models. There is a general tendency for an amplification of the seasonal cycle of rainfall in the West Pacific Monsoon region, as shown by the projected changes in average monthly rainfall over both the three monsoon regions (Southern Hemisphere box-1, Southern Hemisphere box-2 and Northern Hemisphere, as defined in Section 2.5.3), relative to the 20th century multi-model mean (Figure 6.19). There is fairly strong model agreement on the amplification as indicated by the shaded areas. Interestingly, models simulate this amplification only during the initial phase of the wet season in the Northern Hemisphere region while the Southern Hemisphere box-1 region has a consistent increase throughout the wet season, and the Southern Hemisphere box-2 region has a consistent increase for the entire year. The latter result is consistent with the fact that Southern Hemisphere box-2 lies at the eastern edge of the monsoon affected region and receives high rainfall throughout the year.

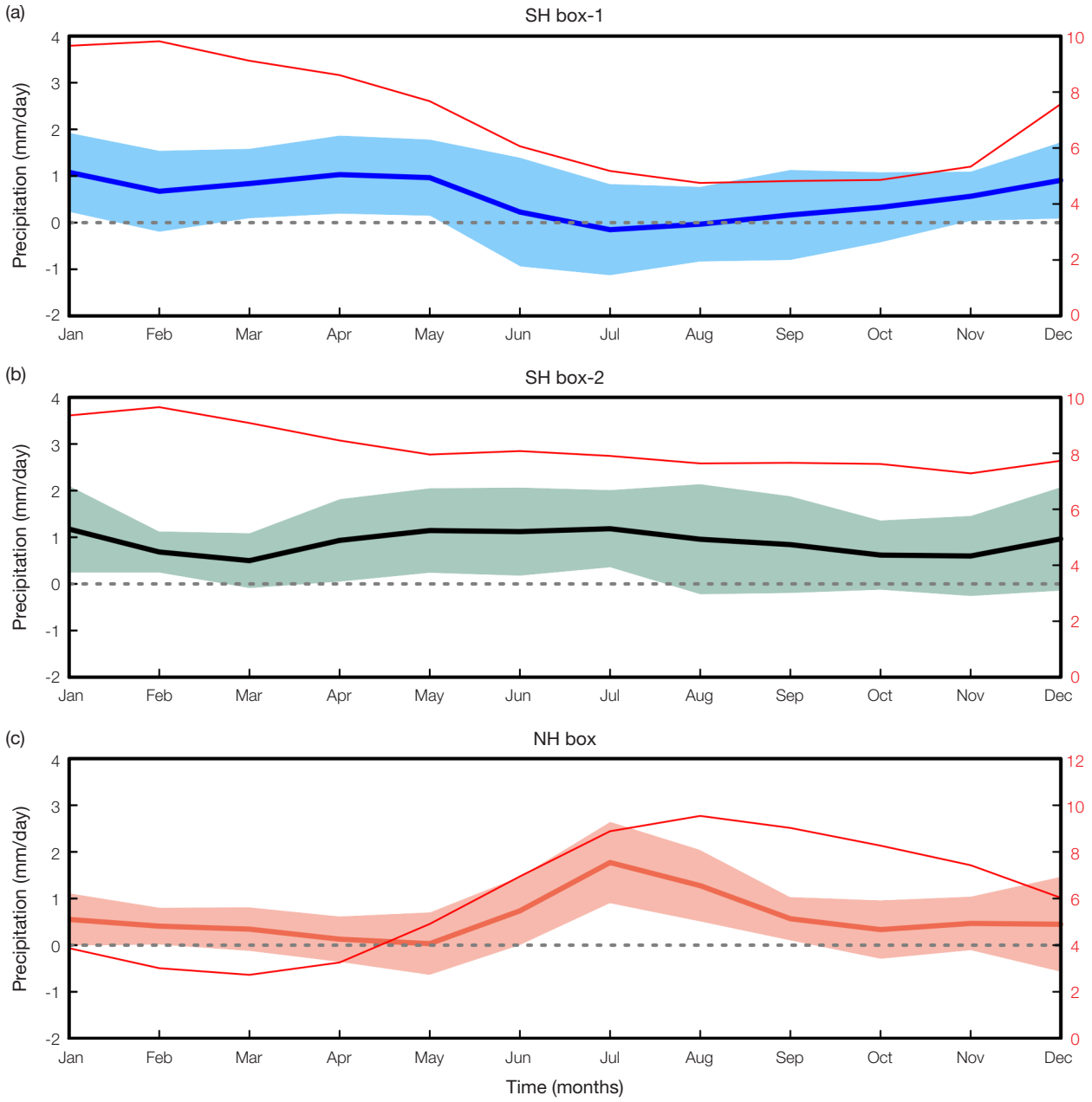

Figure 6.19: Projected changes in average monthly rainfall (mm per day) over the three monsoon regions (SH box-1, SH box-2 and NH, as defined in Section 2.5.3) for 2090, relative to 1990. The multi-model mean for the A2 (high) scenario is shown as the solid thick line; the shaded regions encompass the spread (standard deviation) of the individual model simulations. Also shown is the 20th century annual cycle in red (relating to the right y-axis).

Simulated changes in both low level zonal winds and rainfall in the Southern Hemisphere box-1 region under the A2 (high) emissions scenario from 14 CMIP3 climate models are shown in Figure 6.20. The changes refer to the difference between the two periods (2080–2099) and (1980–1999). This shows that the projected changes favour increases in rainfall while at the same time there is little evidence for a consistent weakening or strengthening of the accompanying low level winds.

As noted previously, monsoon variability is also strongly tied to ENSO, with drought risk increasing during El Niño events, but there is little agreement among climate models with respect to how future climate change may alter the frequency or intensity of El Niño events (Section 6.4.1).

6.4.5 South Pacific Convergence Zone

Future rainfall increases in Pacific region climate are projected to be greatest in the regions of the tropical convergence zones, due to increased atmospheric moisture transport, with the multi-model average change in rainfall showing an increase in the western and central South Pacific, and a decrease in the eastern South Pacific (Christensen et al., 2007). Changes in the position of the SPCZ have been observed in recent decades (Chapter 3), but there is evidence that these may be related to the Interdecadal Pacific Oscillation rather than anthropogenic climate warming (Griffiths et al., 2003).

For the PCCSP study, changes in the SPCZ position and intensity were examined for 16 global climate model simulations, driven by the A2 (high) emissions scenario (Brown et al., in press). The analysis focuses on December-February, when the SPCZ is most intense. The sample of models examined is the same as for other atmospheric projections, except that MIROC3.2(medres) is excluded as this model does not produce a well defined SPCZ (Brown et al., 2011).

Using a simple linear fit to the position of the SPCZ, based on the band of maximum rainfall, the December-February seasonal mean position of the SPCZ is calculated for the last two decades of the 20th century, and compared with the last two decades of the 21st century (Figure 6.21). There is no systematic northward or southward shift in the mean position of the SPCZ, and no systematic shift in the slope of the SPCZ line. One model shows a large increase in the SPCZ slope and a southward shift in latitude due to a change in the width and eastern extent of the SPCZ, and another model shows a northward shift of the SPCZ (see Brown et al., (in press) for details of individual models).

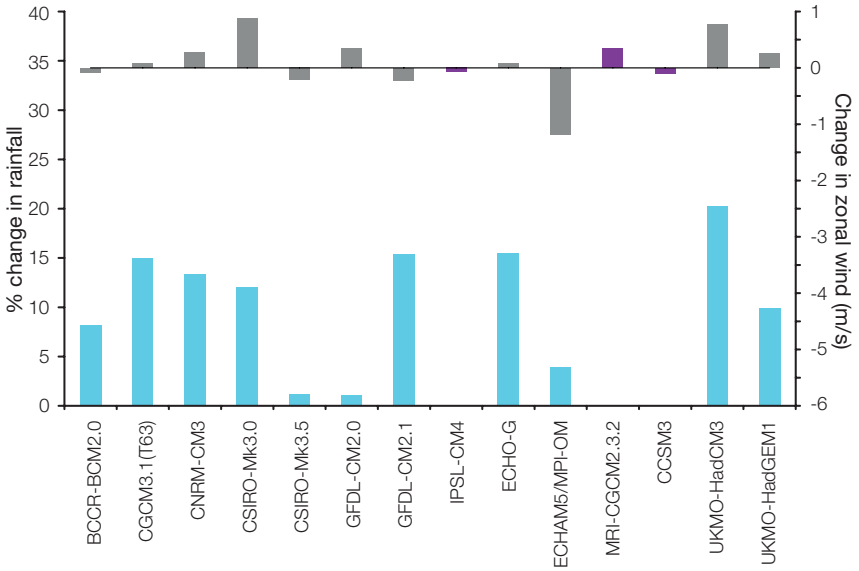

Figure 6.20: Projected changes in December-February zonal (east-west) wind speed (metres per second) and rainfall (%) for the Southern Hemisphere box-1 region (defined in Section 2.5.3) from 14 CMIP3 model results for the A2 (high) emissions scenario. The 1980–1999 mean low level zonal wind-speeds are indicated by the purple bars, while the wind-speed changes (2080–2099 minus 1980–1999) are indicated by the dark grey bars. The accompanying percentage differences in rainfall are indicated by the blue bars.

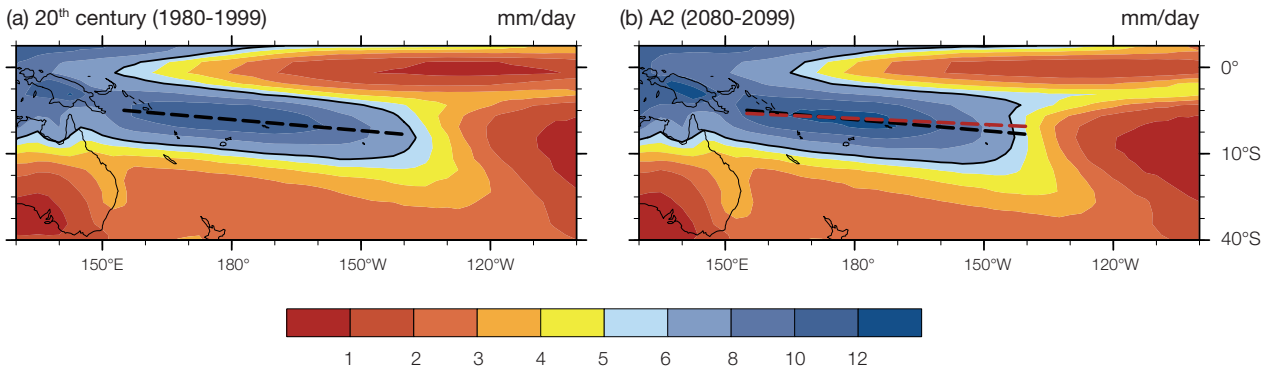

Figure 6.21: The 16 model mean position of the SPCZ in the late 20th and 21st centuries (A2 (high) emissions scenario), as defined by December-February rainfall (mm per day). The black contour shows the 6 mm per day rainfall threshold, giving the approximate edge of the SPCZ. The black dashed line indicates the position of maximum rainfall during 1989–1999, while the red dashed line indicates the position during 2080–2099 for the A2 (high) emissions scenario. See Brown et al., (2011) for details of linear fit method.

Using the 6 mm per day rainfall threshold to define the edge of the SPCZ, changes in the area and intensity of the SPCZ are also calculated. In December-February, the area of the SPCZ increases in the A2 (high) emissions simulations in all models. The majority of models also show an increase in the mean and maximum rainfall within the SPCZ. Overall, there is evidence for more intense SPCZ rainfall in December-February, which is consistent with a stronger hydrological cycle and increased moisture transport in a warmer climate.

At the eastern edge of the SPCZ, between around 150°W to 120°W, there is a decrease in December-February mean rainfall in most models (see Brown et al., in press) and in the multi-model mean (Figure 6.21). This reduction is associated with a relatively small sea-surface temperature increase in the region of the southern sub-tropical anticyclone, and strengthened surface trade winds in this region. The eastern edge of the SPCZ thus appears to contract westwards in the climate change simulations.

Therefore, during December-February, there is a consistent increase in mean and maximum SPCZ rainfall and in the area of the SPCZ in the wet season, with the SPCZ rainfall band becoming wider in most models. There is also a consistent westward contraction of the eastern edge of the SPCZ, associated with a stronger circulation and reduced surface wind convergence in the region to the east of around 150°W in this season. However, there is no consistent shift in the position or slope of the SPCZ in the wet season.

During May-October, the SPCZ in the current climate is generally weaker and closer to the equator than in December-February (Chapter 2 and Chapter 5). In the future, most models project an increase in rainfall within the SPCZ during May-October, with the largest increases on the equatorward side, leading to a shift in the SPCZ towards the equator.

Most CMIP3 models do not accurately simulate the observed diagonal orientation of the SPCZ or the extension of SPCZ rainfall into the extra-tropics in December-February or May-October (Chapter 5). Therefore, the regional-scale changes in rainfall and winds associated with the SPCZ may not be correctly located in the model projections.

6.5 Sea-Level Rise

Projections of sea-level rise require consideration of ocean thermal expansion, the melting of glaciers and ice caps, the surface mass balance and dynamic response of the ice sheets of Antarctica and Greenland, and any changes in storage of water in dams, (Section 4.7). Summaries of sea-level rise issues and recent results can be found in Church et al. (2001), Meehl et al. (2007b), Church et al. (2008, 2010), Milne et al. (2010), Slangen et al. (2010) and Church et al. (2011).

6.5.1 Intergovernmental Panel on Climate Change Projections of Global Averaged Sea-Level Rise for the 21st Century

The projections of the global average sea-level rise by the IPCC Fourth Assessment Report (IPCC 2007; Meehl et al., 2007b) are comprised of two sets of contributions and are for 2090–2099 compared with the average over 1980–1999. The first set includes contributions from ocean thermal expansion, the melting of glaciers and ice caps, the Greenland and Antarctic ice sheet surface mass balances, and the slow dynamic response included in current ice sheet models (Table 6.2). These contributions can be estimated with currently available coupled ocean-atmosphere models and models used to represent the response of land ice to changing atmospheric conditions. The projected ranges given, for the 5% to 95% confidence limits, are from 18 to 38 cm for the B1 (low) emissions scenario to 26 to 59 cm for the A1FI (very high) emission scenario (Meehl et al., 2007b) (Section 5.2.2.6).

In addition, the IPCC Fourth Assessment recognised that these models did not include uncertainties in climate-carbon cycle feedbacks and that there was insufficient understanding to accurately quantify the contribution that might come from any rapid change in ice discharge from the Greenland and Antarctic ice sheets (termed rapid ice here). Using simple scaling arguments, they suggested that the above estimates could increase by up to about 20 cm (17 cm in Table 6.2). However, they recognised that larger values cannot be excluded but that understanding of the relevant processes was "too limited to assess their likelihood or provide a best estimate or an upper bound for sea-level rise" (IPCC, 2007). The sum of all of these contributions to estimate the total sea-level rise is given in Figure 6.22 (see Church et al., 2011 for more details) with the total range across scenarios of about 18 to 80 cm.

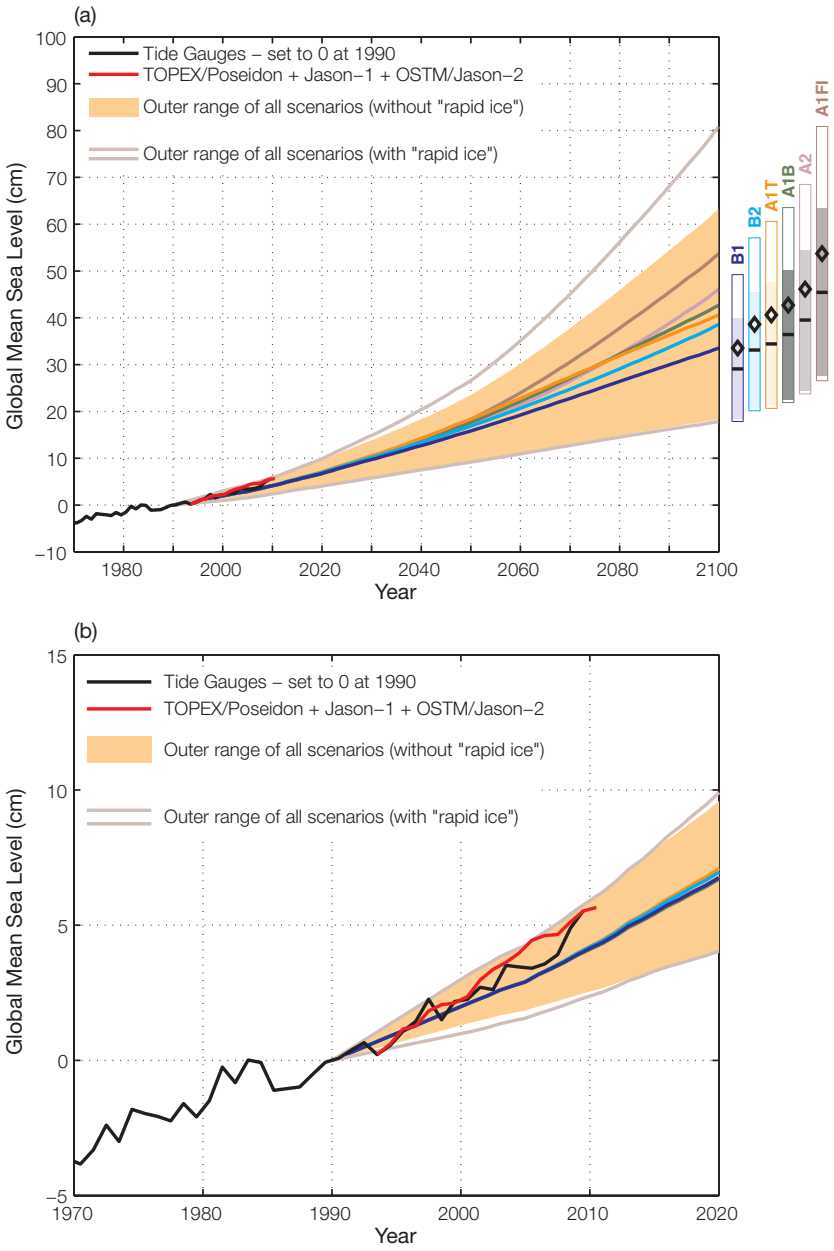

Figure 6.22: Global averaged projections of sea-level rise for six IPCC greenhouse gas emissions scenarios to (a) 2100 and (b) 2020 with respect to 1990. The full range of projections without (with) any rapid ice component is shown by shaded region (outer light lines). The continuous coloured lines from 1990 to 2100 are the central value of the projections including the rapid ice contribution. The bars at the right in (a) are the range of projections in 2100 for the various named scenarios. The horizontal lines (diamonds) in the bars are the central values without (with) the rapid ice sheet contribution. The observational estimates of global averaged sea level estimated from tide gauges and the satellite altimeter data are shown in black and red respectively. The tide gauge data is set to zero at the start of the projections in 1990 and the altimeter data is set equal to the tide gauge data at the start of the record in 1993. The projections are based on the IPCC Fourth Assessment results. From Church et al. (2011).

Table 6.2: The IPCC Fourth Assessment projections of global average sea-level rise during the 21st century and its components under six IPCC emissions scenarios. The upper row in each pair gives the 5 to 95% range (m) of the rise in sea level between 1980–1999 and 2090–2099. The lower row in each pair gives the range of the rate of sea-level rise (mm per year) during 2090–2099. The land ice sum comprises glaciers and ice caps and ice sheets, including dynamics, but excludes the scaled-up ice sheet discharge (see text) which is given separately in line G. The sea-level rise comprises thermal expansion and the land ice sum. Note that for each scenario the lower (upper) bound for sea-level rise is larger (smaller) than the sum of the lower (upper) bounds of the contributions, since the uncertainties of the contributions are largely independent. Reproduced from Meehl et al. (2007b).

		B1		B2		A1B		A1T		A2		A1FI	
A.Thermal expansion	m	0.10	0.24	0.12	0.28	0.13	0.32	0.12	0.30	0.14	0.35	0.17	0.41
	mm/yr	1.1	2.6	1.6	4.0	1.7	4.2	1.3	3.2	2.6	6.3	2.8	6.8
B. Glacial and ice cap	m	0.07	0.14	0.07	0.15	0.08	0.15	0.08	0.15	0.08	0.16	0.08	0.17
	mm/yr	0.5	1.3	0.5	1.5	0.6	1.6	0.5	1.4	0.6	1.9	0.7	2.0
C. Greenland ice sheet surface mass balance	m	0.01	0.05	0.01	0.06	0.01	0.08	0.01	0.07	0.01	0.08	0.02	0.12
	mm/yr	0.2	1.0	0.2	1.5	0.3	1.9	0.2	1.5	0.3	2.8	0.4	3.9
D. Antarctic ice sheet surface mass balance	m	-0.10	-0.02	-0.11	-0.02	-0.12	-0.02	-0.12	-0.02	-0.12	-0.03	-0.14	-0.03
	mm/yr	-1.4	-0.3	-1.7	-0.3	-1.9	-0.4	-1.7	-0.3	-2.3	-0.4	-2.7	-0.5
E = B + C + D.	m	0.04	0.18	0.04	0.19	0.04	0.20	0.04	0.20	0.04	0.20	0.04	0.23
Land ice sum	mm/yr	0.0	1.8	-0.1	2.2	-0.2	2.5	-0.1	2.1	-0.4	3.2	-0.8	4.0
F = A + E.	m	0.18	0.38	0.20	0.43	0.21	0.48	0.20	0.45	0.23	0.51	0.26	0.59
Sea level rise	mm/yr	1.5	3.9	2.1	5.6	2.1	6.0	1.7	4.7	3.0	8.5	3.0	9.7
G. Scaled-up ice sheet discharge	m	0.00	0.09	0.00	0.11	-0.01	0.13	-0.01	0.13	-0.01	0.13	-0.01	0.17
	mm/yr	0.0	1.7	0.0	2.3	0.0	2.6	0.0	2.3	-0.1	3.2	-0.1	3.9

6.5.2 Post-Intergovernmental Panel on Climate Change Fourth Assessment Results

Recent results (since 2007) indicate an increased contribution over the past decade from glaciers and ice caps (Cogley, 2009) and the ice sheets (Velicogna, 2009; Rignot et al., 2011). In particular, discharge from glaciers and ice streams of the Greenland and Antarctic ice sheets are showing signs of a dynamic response, potentially leading to a more rapid rate of rise than can occur from surface melting alone. Using kinematic constraints, Pfeffer et al. (2008) estimated that sea-level rise greater than 2 m by 2100 was physically untenable and that a more plausible estimate was about 80 cm, consistent with the upper end of the IPCC estimates and the present rate of rise. This value still requires a significant acceleration of the ice sheet contributions.

The last two IPCC assessments and recent publications (Rahmstorf et al., 2007; Church et al., 2011; Figure 6.22b) indicate the rate of sea-level rise is currently near the upper limit of the projections (including the scaled-up ice discharge). This does not imply that sea level will continue to follow this upper limit. This observation has raised concern that the IPCC projections may be underestimates, especially given the current inability to adequately model the ice sheets' response to global warming, and has led to the development of several semi-empirical models of sea-level rise (Rahmstorf, 2007; Horton et al., 2008; Grinsted et al., 2009; Vermeer and Rahmstorf, 2009). These semi-empirical models all give larger rates of rise during the 21st century (upper values as high as 1.8 m) than the Fourth Assessment projections. However, significant concerns have been raised about the robustness of these projections on several grounds (Holgate et al., 2007; Schmith et al., 2007; Lowe and Gregory, 2010; Church et al., 2011) and they should be used with caution until these limitations are more fully understood.

A recent comprehensive study exploring high-end climate change scenarios for flood protection in the Netherlands (Vellinga et al., 2009; Katsman et al., in press) did not adopt these semi-empirical models and instead suggested a global-averaged upper-end sea-level rise scenario of 0.55 to 1.1 m by 2100.

Improved understanding of the processes responsible for ice sheet changes are urgently required to improve estimates of the rate and timing of 21st century and longer-term sea-level rise. This understanding is developing rapidly, and early results (Joughin et al., 2010) are consistent with the IPCC Fourth Assessment projections. However, there are not yet robust projections of the dynamic response of the Greenland and Antarctic ice sheets for the 21st century or beyond. The next IPCC report is likely to contain substantially improved assessment of potential ice sheet contributions.

6.5.3 Regional Distribution of Sea-Level Rise During the 21st Century

The regional distribution of sea-level rise is important because it is the regional or local sea-level change and local land motion that most directly impacts society and the environment. Satellite-altimeter data show significant regional variations in the rate of sea-level rise (Figure 3.20), with some regions having experienced substantially larger rates than the global-averaged rate of rise since 1993. However, this regional variation in the relatively short altimeter record is at least partly a result of climate variability, particularly in the equatorial Pacific Ocean.

During the 21st century, there will be two significant reasons for the departure of regional sea-level change from the global averaged rise (Figure 6.23). These are associated with climate and ocean variability and the associated ocean dynamics, and the changing distribution of water on the Earth (Section 4.7). The latter changes the surface loading of the Earth and thus the vertical motion of the surface of the Earth, and also changes the gravitational field thus changing the regional height of the ocean surface.

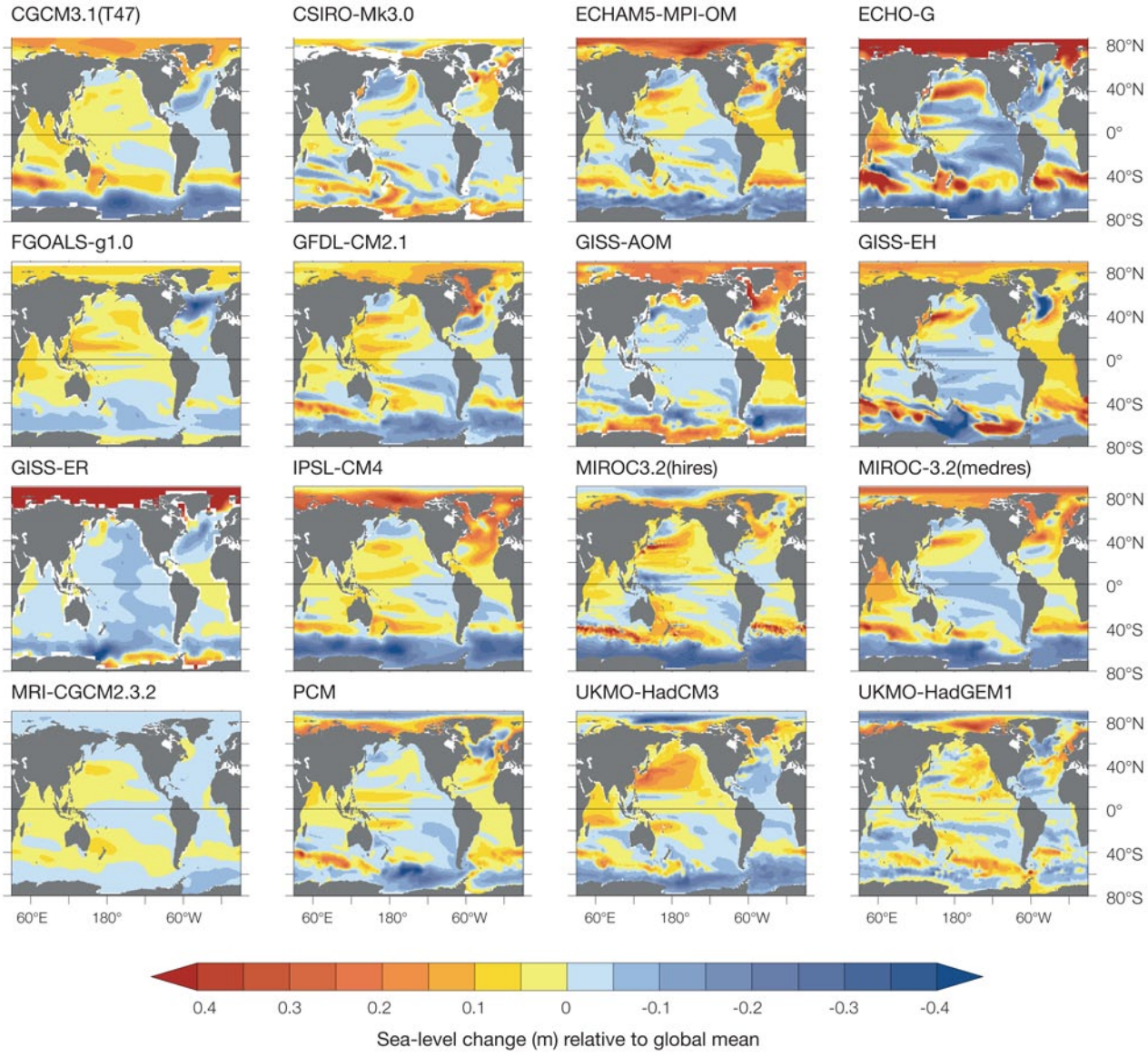

Figure 6.23: The global distribution of sea-level rise (m) in 16 models available from the CMIP3 experiment for the A1B (medium) scenario. The global mean sea-level rise has been subtracted from each panel and the rise is for the 2081–2100 period compared with the 1981–2000 period.

6.5.3.1 Ocean Dynamical Changes

On a global scale, the response of sea-levels to global warming is not spatially uniform (Figures 6.23 and 6.24), with some regions experiencing higher or lower sea-level change than the global average.

The regions where global climate models tend to agree with each other on future sea-level change for the period 2081–2100 compared with 1981–2000 occupy only a small percentage of the globe. However, there are some common features in the model responses. Within the tropical Pacific, two-thirds of the models indicate that sea-level rise is lower than the global-averaged rise in a band running from Papua New Guinea to southern South America, i.e. most of south-easterly trade winds prevailing regions (Figure 6.24). Slightly higher sea-level change can be found in the region east of Australia and in the eastern Indian Ocean. Such regional patterns of sea-level change can be mainly attributed to regional wind-stress changes and the resultant vertical movement of the thermocline, especially the intensification of south-easterly trade winds. Wind stress changes cause a vertical movement of the water column (and hence changes in density) through Ekman dynamics and Rossby wave dynamics (Qiu and Chen, 2006; Timmermann et al., 2010). Wind-stress change can also induce gyre-circulation change, such as the barotropic circulation from Sverdrup theory (Sverdrup, 1947), though such barotropic gyre-circulation change usually has secondary effects on sea-level change, especially in low-latitudes (Lowe and Gregory, 2006). The intensification of south-easterly winds is related to the regional patterns of sea-surface temperature change in the tropical South Pacific with maximum warming on the equator and minimum warming in the south-eastern tropical Pacific. Thus the regional sea-level change in the tropical Pacific is part of complex ocean-atmosphere interaction on climate change time scales, as discussed by Timmermann et al. (2010).

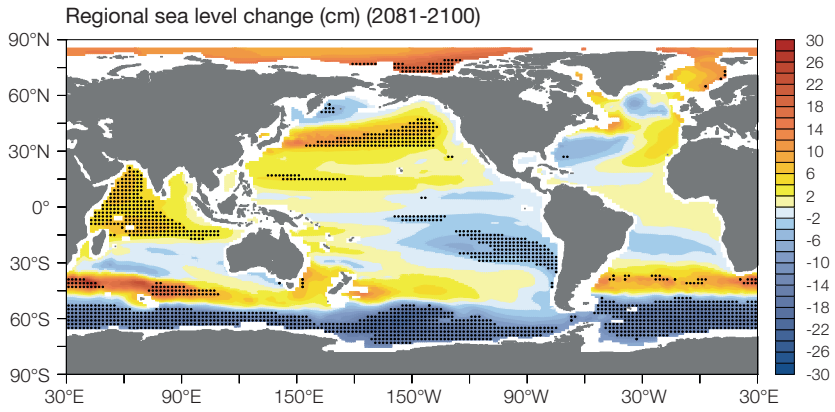

Figure 6.24: The global distribution of regional sea-level change (in cm) due to ocean density and circulation change during 2081–2100 relative to 1981–2000, derived from 13 available CMIP3 models subjected to the A1B (medium) scenario. The global mean is removed, thus positive (negative) values indicate higher (lower) local sea-level change than global average. Stippling denotes that regions where climate models tend to agree, defined as the regions where the magnitude of multi-model mean exceeds the inter-model standard deviation.

The spatial standard deviation (relative to the global average) of multi-model mean of sea-level change relative to period 1981–2000 under the A1B (medium) scenario is 0.032, 0.056 and 0.083 metres globally for the periods 2021–2040, 2046–2065 and 2081–2100, respectively (refer to Figure 6.25 for tropical Pacific), which implies the spatial variability in the pattern of regional sea-level change increases over the next 100 years (Pardeans et al., 2010; Yin et al., 2010).

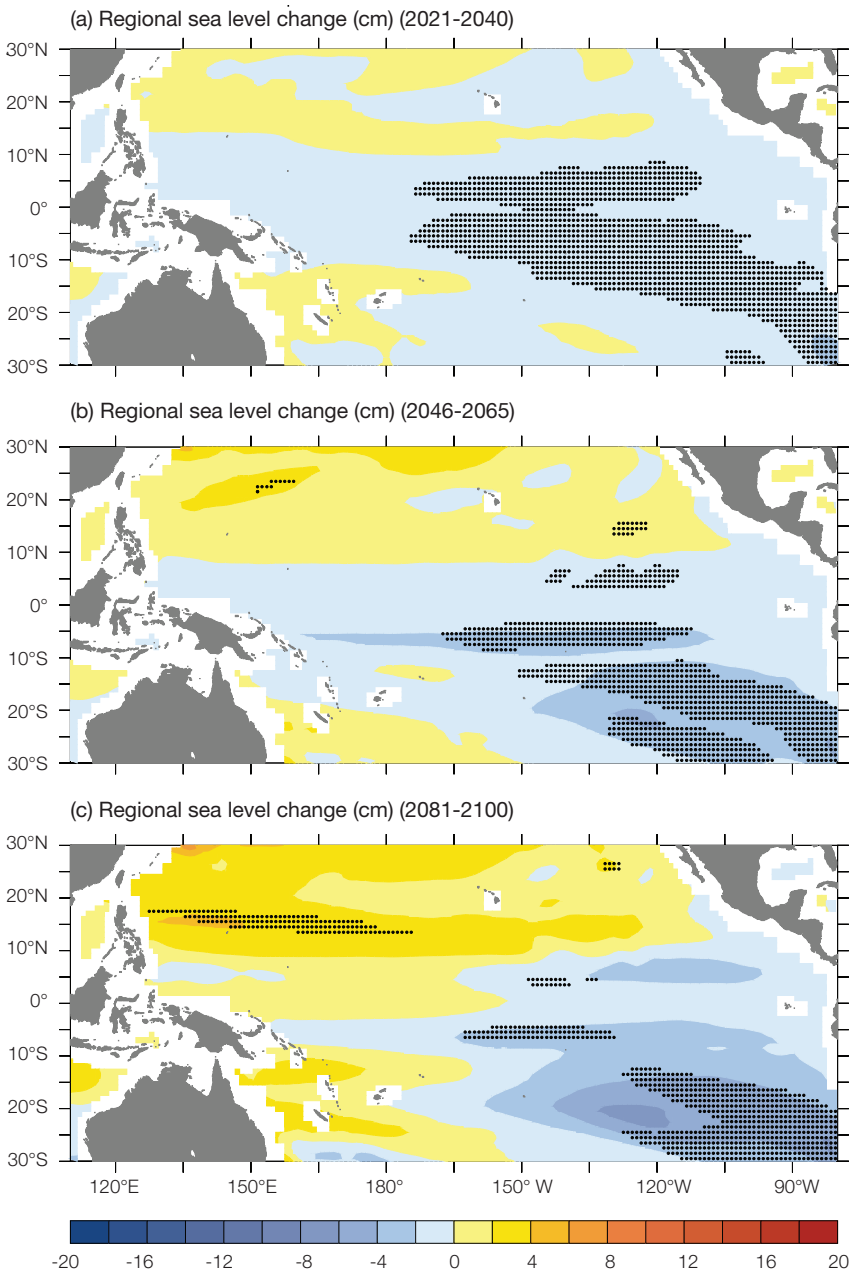

Figure 6.25: Regional sea-level change (in cm) for the PCCSP region due to ocean density and circulation change during (a) 2021–2040, (b) 2046–2065 and (c) 2081–2100 relative to 1981–2000, derived from 13 available CMIP3 models subjected to the A1B (medium) scenario. The global mean is removed, thus positive (negative) values indicate higher (lower) local sea-level change than global average. Stippling denotes regions where climate models tend to agree, defined as the regions where the magnitude of multi-model mean exceeds the inter-model standard deviation.

Regional dynamic sea-level change patterns simulated by CMIP3 climate models can be mostly explained by regional steric sea-level change calculated over the full ocean depth (Figure 6.26). Steric sea-level change is derived from the vertical integral of sea water density change, which can be further divided into a thermosteric component (i.e. associated with temperature change) and halosteric component (i.e. associated with salinity change). For global mean steric sea-level change, the thermosteric component plays a dominant role, while the halosteric component has a minor role (Church et al., 2010). Nonetheless, both components have comparable effects in regional sea-level change distributions, and tend to compensate each other in many regions (Figure 6.26; Yin et al., 2010). Though thermosteric sea-level change is positive almost everywhere (Landerer et al., 2007), thermal expansion in the tropical Pacific is generally less than the global average, by about -4 to -6 cm (Figure 6.26). Both the global hydrological cycle change and ocean circulation change (especially the Atlantic Meridional Overturning Circulation) redistribute salt among different basins and thus lead to halosteric sea-level change (Yin et al., 2010). The tropical and North Pacific are projected to be fresher and have a halosteric sea-level change of about +4 to +6 cm (Figure 6.26). However, while progress is being made, there is still insufficient understanding of what controls the regional pattern of steric sea-level rise.

Superimposed on the long-term trends in sea level are interannual and decadal variations (as discussed in Chapter 3) which will continue into the future. Coastal communities will be impacted by the combination of the long-term sea-level rise, the natural variability in sea level and of course extreme sea-level events caused by storms and waves.

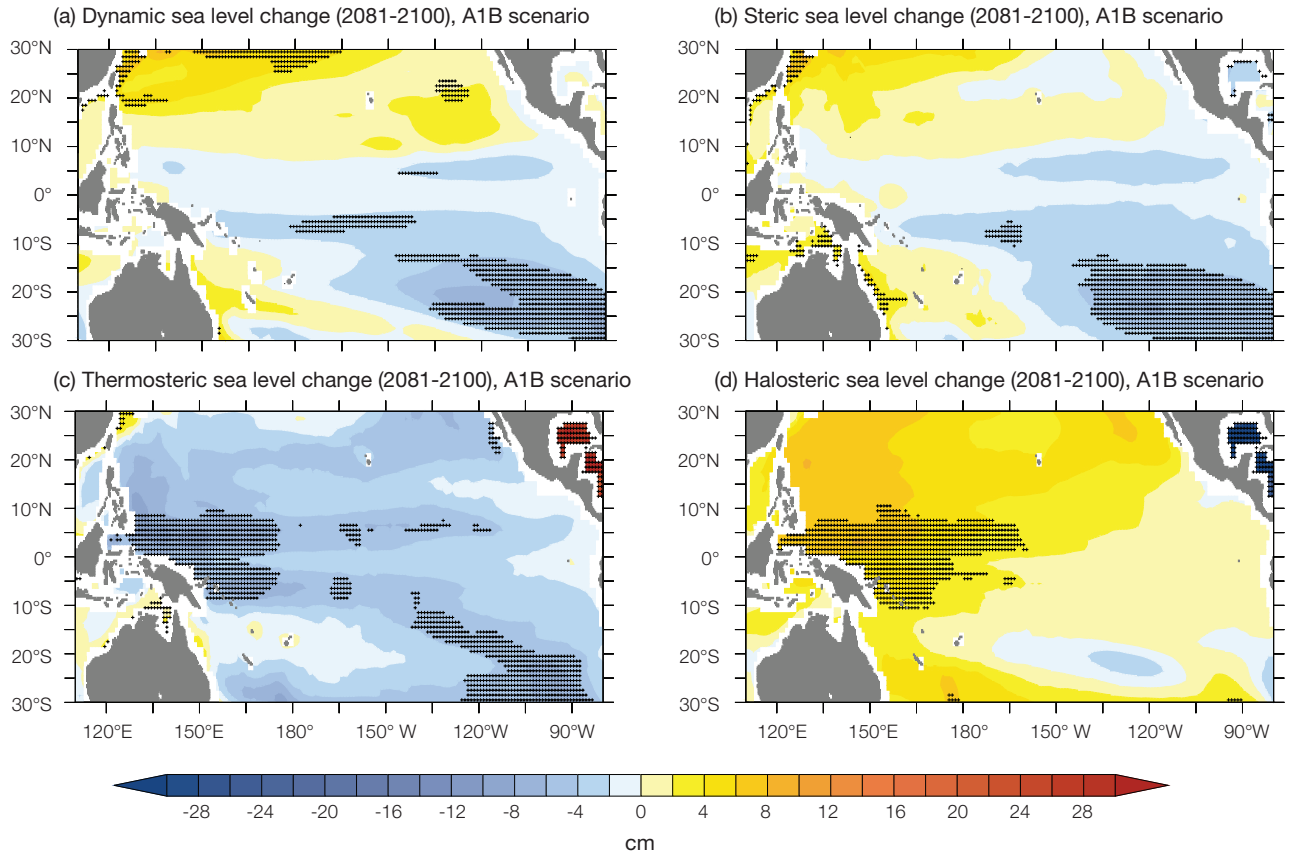

Figure 6.26: (a) Regional dynamic sea-level change (in cm) for the PCCSP region due to ocean density and circulation change during 2081–2100 relative to 1981–2000, derived from 13 available CMIP3 models subjected to the A1B (medium) scenario. (b) Steric (c) thermosteric and (d) halosteric sea-level change (in cm) over full ocean depth during 2081–2100 relative to 1981–2000, derived from 11 available CMIP3 models subjected to the A1B (medium) scenario. The global mean is removed from each panel, thus positive (negative) values indicate higher (lower) local sea-level change than global average. Stippling denotes that regions where climate models tend to agree, defined as the regions where the magnitude of multi-model mean exceeds the inter-model standard deviation.

6.5.3.2 Ocean Mass Changes

In addition to changes in ocean conditions, changes in the mass of the ice sheets (and glaciers and ice caps) also influence the regional distribution of sea-level rise through corresponding changes in the Earth's gravitational field and the elastic movement of the Earth's crust, called sea-level fingerprints (Mitrovica et al., 2001, 2009). As a result, the contribution from the ice sheets implies a lower relative sea level near decaying ice sheets (Greenland and the West Antarctic ice sheets) and a larger than the globally averaged rise (up to about 20–30%) far from the decaying ice sheets. Gomez et al. (2010) demonstrates that these regional distributions may be an important stabilisation factor for the ice sheets because of a local sea-level fall. Ice sheet contributions to future sea-level rise may have a disproportionate impact in some far-field regions. Indeed, in the PCCSP region, contributions from the glaciers and ice caps, and the Greenland and Antarctic ice sheets are all about 20% above the global average rise from each of these contributions (Mitrovica et al., 2001, 2009).

6.5.3.3 Total Regional Sea Level Change

In various studies, the global averaged sea-level rise has been combined with the ocean dynamical response and these regional fingerprints make regional projections of sea-level rise for particular regions (Katsman et al., in press) and worldwide (Kopp et al., 2010; Slangen et al., 2010).

PCCSP scientists have combined global averaged sea-level rise from coupled atmosphere-ocean models with the regional changes resulting from ocean dynamics and mass redistribution and regional fingerprints to estimate the total regional sea-level change for the tropical and sub-tropical Pacific region for the A1B (medium) emissions scenario. The small local ongoing response of the solid Earth to changes since the last glacial maximum has not been included (Church et al., 2011; Figure 6.27). The glacier and ice sheet fingerprint was calculated assuming that the spatial pattern of mass loss to the ocean in the 21st century had a similar pattern to that from 1993 to 2007 (Cogley, 2009). The surface mass balance changes over Greenland and Antarctica were assumed uniform.

One-third of the rapid ice contribution was assumed to come from Greenland and two-thirds from the West Antarctic ice sheet. The total projections of sea-level change (Figure 6.27) are non-uniform with a slightly above global average rise in the western Pacific and Indian Oceans and in a band extending around the oceans at about latitude 40°S. For the PCCSP region (Figure 6.28), the less than global average ocean dynamical sea-level rise and the larger than average sea-level rise as a result of the gravitational/elastic responses counteract such that the total sea-level rise is similar to the global average. Similar patterns are calculated for other greenhouse gas scenarios and time frames.

In addition to the regional changes associated with present day changes in mass there are ongoing changes in relative sea level associated with changes in surface loading over the last glacial cycle (glacial isostatic adjustment) and local tectonic motions. The glacial isostatic motions are relatively small for the PCCSP region.

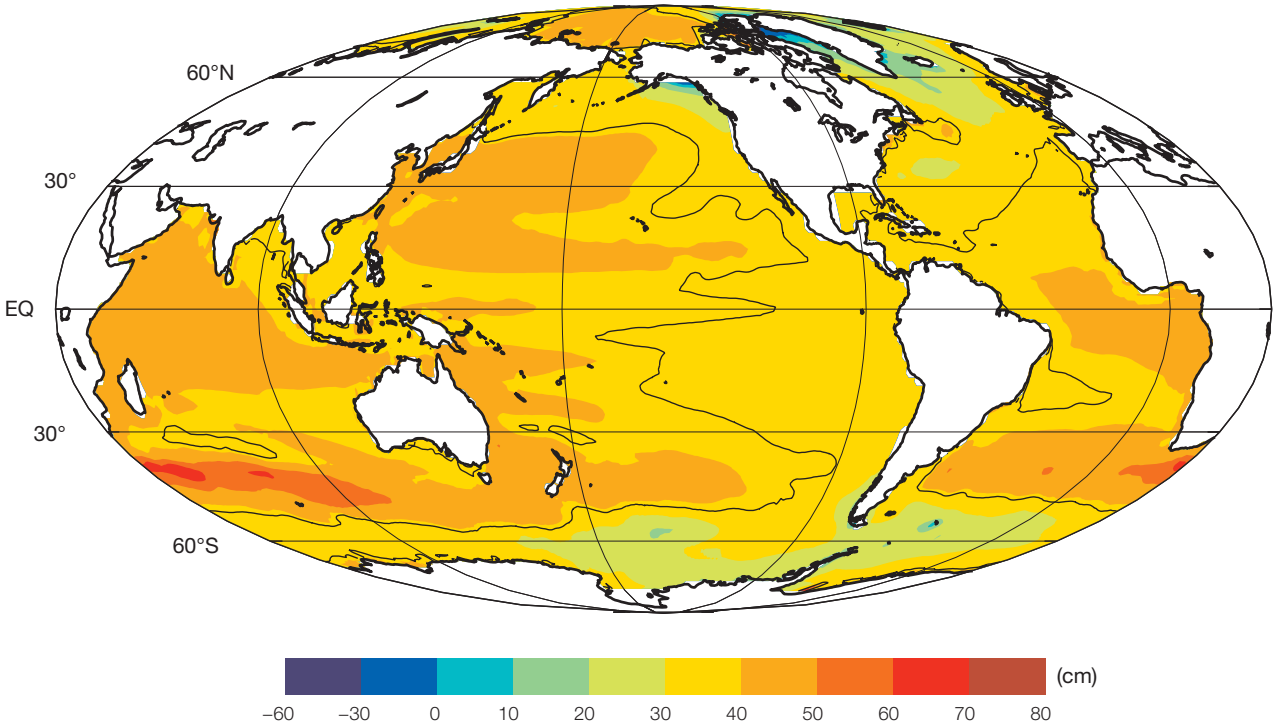

Figure 6.27: The regional distribution of the projections of sea-level change for 2090 compared to 1990, combining the global average sea-level projections, the dynamic ocean departure from the global average and the regional changes associated with the changing mass distribution in the cryosphere for the A1B (medium) scenario. The black contour is the average value at 2090 of 38 cm dividing those regions with above and below average sea-level rise. From Church et al. (2011).

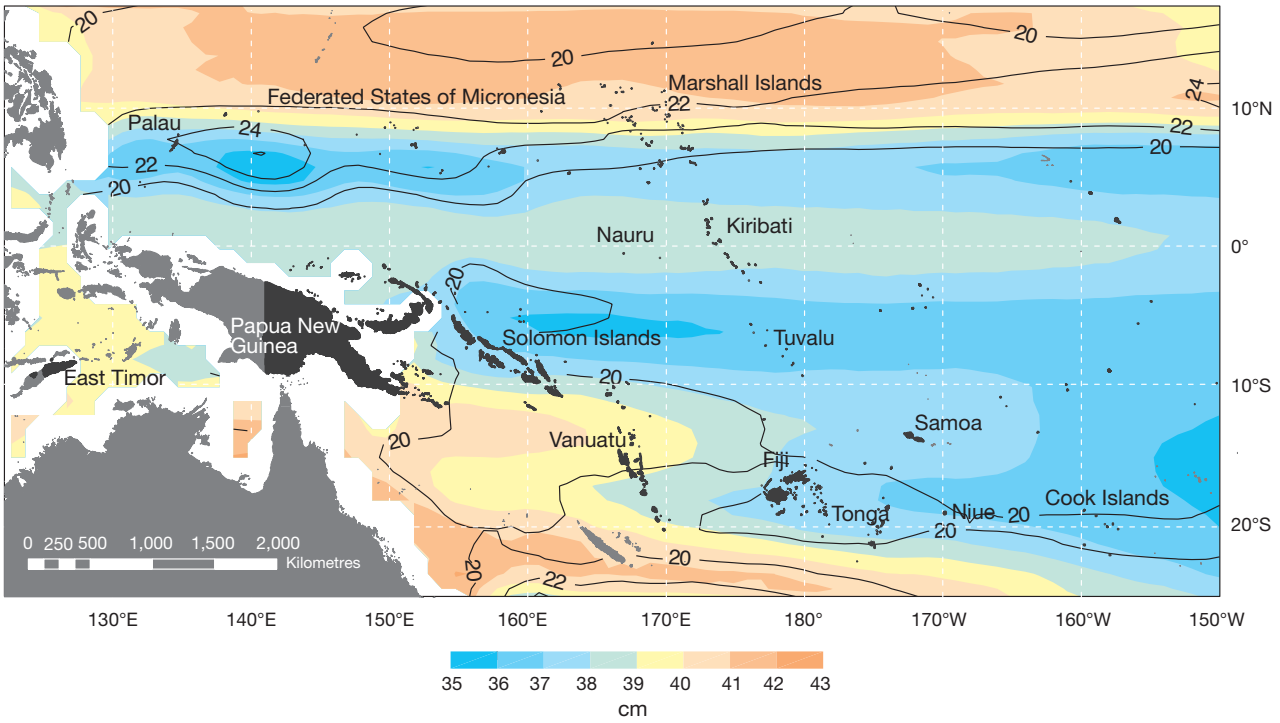

Figure 6.28: The sea-level projections (in cm) for the A1B (medium) emissions scenario in the PCCSP region for 2081–2100 relative to 1981–2000 are indicated by the shading, with the uncertainty indicated by the contours. The distribution of the projections of sea-level change are estimated by combining the global average sea-level projections, the dynamic ocean departure from the global average and the regional changes associated with the changing mass distribution in the cryosphere.

6.5.4 Sea-Level Rise Beyond 2100

It is critically important to recognise that the oceans and the ice sheets take a long time to respond to changes in climate. As a result, sea-level rise will continue for centuries after 2100.

Glaciers and ice caps (outside the polar regions) contain a limited mass of ice (less than about 50 cm of equivalent sea-level rise if they were all to melt (Radic and Hock, 2010)), so their contribution to sea-level rise is limited. However, ocean thermal expansion will continue for centuries, even after greenhouse gas concentrations in the atmosphere have been stabilised, due to the slow transfer of heat from the surface to the deep ocean. The eventual sea-level rise would be dependent on the concentration of greenhouse gases and atmospheric temperatures; climate model simulations suggest of the order of 0.5 m per degree Celsius of global warming (Meehl et al., 2007b).

The Antarctic and Greenland ice sheets are the biggest concerns for longer-term sea-level rise. The area and mass of melt from the Greenland ice sheet (which contains enough water to raise sea level by about 7 m) is increasing. Model simulations indicate that surface melting of the Greenland ice sheet will increase more rapidly than snowfall, leading to a threshold in temperature above which there is an ongoing decay of the Greenland ice sheet over millennia. This threshold is estimated as a global-averaged temperature rise of just 3.1 ± 0.8°C (one standard deviation) above pre-industrial temperatures (Gregory and Huybrechts, 2006). With unmitigated emissions of greenhouse gases, the world is likely to pass this threshold during the 21st century, committing the world to metres of sea-level rise, although from surface melting alone this would take millennia. The Antarctic ice sheet presently experiences little surface melting and its contribution to sea level is dependent on changes in the surface mass balance and the currently uncertain dynamic response.

6.6 Ocean Acidification

Ocean acidification results from the net uptake of CO_2 released to the atmosphere through human activities. The net uptake causes a decline in seawater pH and a decrease in dissolved carbonate ion concentrations (Feely et al., 2004). The decrease in carbonate ion concentrations leads to a lowering of the seawater saturation state of carbonate minerals (Feely et al., 2009), including aragonite, which is the form of calcium carbonate precipitated by reef building corals and many other key reef organisms (Guinotte and Fabry, 2008). Studies indicate that coral growth rates typically decline as the aragonite saturation state of waters decrease with potential to impact the growth of coral reef ecosystems (Langdon and Atkinson, 2005). Other calcifying organisms may also be impacted leading to weaker reef structures (Manzello et al., 2008), greater susceptibility to external stresses like warming (Anthony et al., 2008), and shifts in ecosystems (Hoegh-Guldberg et al., 2008).

Changes in the seawater aragonite saturation state (Figure 6.29) over the 21st century were estimated in the PCCSP region using data from six climate models (CGCM3.1(T47), CNRM-CM3, CSIRO-Mk3.5, GFDL-CM2.0, MIROC3.2 (medres) and UKMO-HadCM3), which are in turn used to drive an offline carbonate chemistry model. The six models are those that had the required projections of salinity and temperature change under low, medium and high emissions scenarios (B1, A1B and A2, respectively). To drive these models three inputs were used: (1) projections of future ocean carbon uptake, (2) empirical relationships between ocean carbonate chemistry and salinity, and (3) projections of temperature and salinity. The future oceanic carbon uptake was derived from projected atmospheric CO_2 concentrations under the different emissions scenarios, observed seasonality in surface partial pressure of CO_2 (Takahashi et al., 2009), and future trends in uptake from the IPSL CM4-LOOP coupled climate carbon model (Marti et al., 2010).

The results show: (1) the key driver for ocean acidification is the atmospheric CO_2 concentration, and the magnitude and rate of ocean acidification is proportional to this concentration; (2) for the first half of this century, the low, medium and high emissions scenarios (B1, A1B and A2, respectively) result in similar atmospheric CO_2 concentrations, and the change in aragonite saturation state for this period is largely independent of the emissions scenario; (3) over the second half of this century, the aragonite saturation state in the entire PCCSP region will continue to decline with the greatest changes occurring under the highest (A2) emission scenario; (4) the lowest values in this century will occur in the eastern equatorial Pacific, to the east of 160°W (the easternmost islands of Kiribati), with the highest values in the region of the South Equatorial Current, between approximately latitudes 5°S and 20°S (Cook Islands, Samoa, Tuvalu).

Marine environments with seawater values of aragonite saturation states greater than 4 are generally considered optimal for coral growth, with values below 3.5 becoming increasingly marginal for sustaining healthy coral growth and reefs (Kleypas et al., 1999; Guinotte et al., 2003). Other calcifying organisms may also be impacted, leading to weaker reef structures (Manzello et al., 2008), greater susceptibility to external stresses like warming (Anthony et al., 2008), and shifts in ecosystems to species more resilient to acidification (Hoegh-Guldberg et al., 2008). As saturation states continue to decline, reef ecosystems could change from conditions of net growth to net dissolution (loss) of carbonate (Silverman et al., 2009).

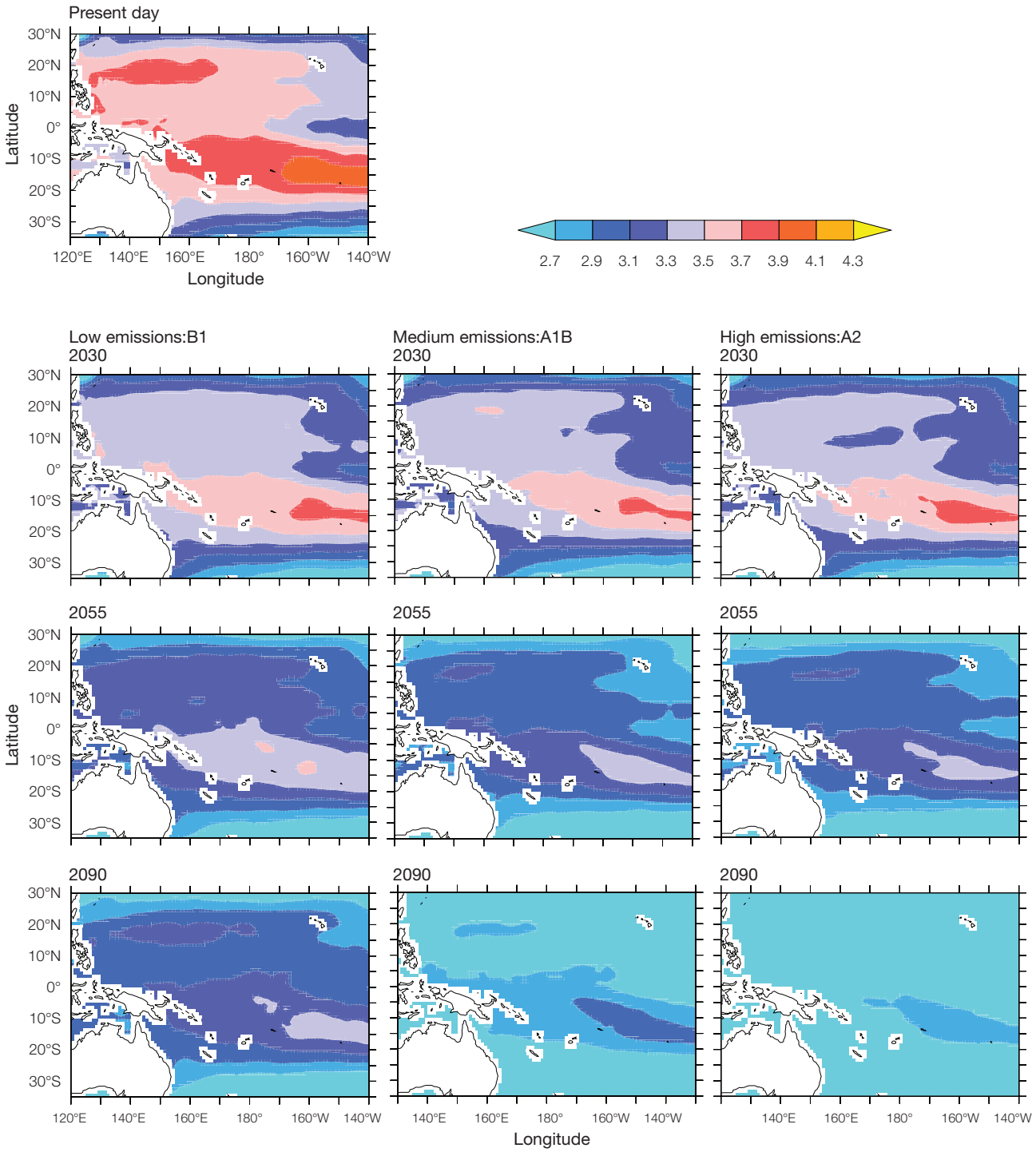

Figure 6.29: The multi-model mean of annual maximum values of aragonite saturation state in surface waters for the present day and in 2030, 2055 and 2090 from six climate models. The B1 (low), A1B (medium) and A2 (high) emissions scenarios are shown.

6.7 Synthesis of Projections

This synthesis of regional projections focuses on multi-model mean changes and may therefore be considered to represent central estimates. For more information at the country-scale regarding the spread of individual model projections, the impact of relevant model deficiencies, physical plausibility, and the consistency of the projections with observed changes over recent decades, see Volume 2. Uncertainties in climate projections are summarised in Box 6.1.

6.7.1 Summary of Atmospheric Projections

Temperature: The projected warming over the PCCSP region is about 70% as large as the global average warming for all emissions scenarios. The projected regional warming is around 0.5–1.0°C by 2030, regardless of the emissions scenario. By 2055, the warming is generally 1.0–1.5°C with regional differences depending on the emissions scenario. By 2090, the warming is generally 1.5–2.0°C for B1 (low) emissions, around 2.0–2.5°C for A1B (medium) emissions, and around 2.5–3.0°C for A2 (high) emissions. Large increases in the incidence of heat waves, extremely hot days and warm nights are also projected.

Rainfall: In the PCCSP region, increases in annual mean rainfall are projected to be most prominent near the SPCZ (affecting the Cook Islands, Fiji, Nauru, Niue, Samoa, the Solomon Islands, Tonga, Tuvalu, Vanuatu and Kiribati) and ITCZ (affecting Federated States of Micronesia, Kiribati, Marshall Islands, Nauru, Palau and Papua New Guinea), with little change in the remainder of the region. The annual numbers of rain days (over 1 mm), light rain days (1–10 mm) and moderate rain days (10–20 mm) are projected to increase near the equator, with little change elsewhere in the region. There is a widespread increase in the number of heavy rain days (20–50 mm). Extreme rainfall events that currently occur once every 20 years on average are generally simulated to occur four times every year by 2055 and seven times every year by 2090 under the A2 (high) scenario. Droughts are expected to occur less often.

Solar radiation: Consistent with the projected rise in annual mean rainfall throughout much of the PCCSP region, solar radiation is projected to decline due to increased cloudiness. The largest decreases in solar radiation occur near the ITCZ and SPCZ.

Humidity: Little change in relative humidity is projected through most of the PCCSP region. This is because while a warmer atmosphere can hold more water vapour, the amount of water vapour in the air can also be expected to increase due to the essentially unlimited supply of moisture from the vast expanses of ocean in the region.

Wind: Surface wind speed generally decreases in the equatorial and northern parts of the PCCSP region, while increases are indicated in the south, but these changes are projected to be relatively small in most locations. Projected changes in wind direction are very small.

Potential evapotranspiration: Increases in potential evapotranspiration are expected. The ratio of annual average rainfall to potential evapotranspiration decreases in most regions (increased aridity), except near Kiribati, Nauru and Tuvalu where the relatively large projected rainfall increases overwhelm the smaller changes in potential evapotranspiration.

6.7.2 Summary of Ocean Projections

Sea-surface temperature: Increases are expected with maximum warming in the central equatorial Pacific and least warming in the south-eastern Pacific. The West Pacific Warm Pool (defined here as temperatures above 29°C) increases in extent, with the edge of the pool moving many thousands of kilometres east along the equator over coming decades.

Sea-surface salinity: Decreases are expected with regional differences closely matching projected changes in rainfall and evaporation. The intensified warming and freshening at the surface is projected to make the surface ocean become less dense compared to the deep ocean, so the ocean becomes more stratified. This increase in stratification acts to inhibit mixing, thereby reducing the supply of nutrients from the deep to the surface ocean, with consequences for biological productivity.

Sea level: Projections of sea-level rise require consideration of ocean thermal expansion, the melting of glaciers and ice caps, the surface mass balance and dynamic response of the ice sheets of Antarctica and Greenland, and changes in terrestrial water storage. Recent results indicate that global-mean sea-level rise greater than 2 m by 2100 is physically untenable and that a more plausible estimate is about 80 cm, consistent with the upper end of the IPCC estimates and the present rate of rise. Other results suggest a global-averaged upper-end sea-level rise scenario of 0.55 to 1.1 m by 2100. However, improved understanding of the processes responsible for ice sheet changes is urgently required to improve estimates of the rate and timing of 21st century and longer-term sea-level rise. For the PCCSP region, the less than global average ocean dynamical sea-level rise and the larger than average sea-level rise as a result of the gravitational/elastic responses, counteract such that the total sea-level rise is slightly larger than the global average.

Ocean acidification: The projected growth in atmospheric CO_2 concentration is expected to cause further ocean acidification. Aragonite saturation values below 3.5 are projected to become more widespread and increasingly marginal for sustaining healthy coral growth and reefs. The lowest values are projected to occur in the eastern equatorial Pacific to the east of 160°W (the easternmost islands of Kiribati), with the highest values in the region of the South Equatorial Current, between approximately latitudes 5°S and 20°S (Cook Islands, Samoa, Tuvalu).

6.7.3 Summary of Projected Changes in Key Climate Features and Variability

El Niño-Southern Oscillation (ENSO): Year-to-year variability in the region will continue to be largely driven by ENSO. Unfortunately, climate models do not provide consistent projections of changes in the frequency, intensity and patterns of future El Niño and La Niña events. As the climate changes, however, some aspects of the climate experienced in some regions during El Niño and La Niña events may differ from what was experienced in the past. For example, if El Niño tends to warm a particular region, then future El Niño events will tend to be warmer than El Niño events experienced in the past.

Indian Ocean Dipole (IOD): Climate models suggest that a more positive IOD-like mean-state will continue with easterly wind trends and a shallowing thermocline over the eastern Indian Ocean, associated with a weakening of the Walker Circulation. Further research is required to assess the degree of consensus amongst models regarding projected changes in IOD frequency and amplitude.

South Pacific Convergence Zone (SPCZ): In the wet season (November-April), the SPCZ is not expected to shift position, but there is some evidence of an equatorward shift in the dry season (May-October). Increased rainfall is projected within the SPCZ in the wet season in particular, due to increased atmospheric moisture content in a warmer climate. Many models also suggest that the eastern edge of the SPCZ will become drier in the wet season as the trade winds in the south-east Pacific become stronger.

Intertropical Convergence Zone (ITCZ): Changes in rainfall averaged over the ITCZ show a general increase in June-August, with little change in December-February, thereby amplifying the current seasonal cycle. There is an increase in the area of the ITCZ in all models in June-August, and in all but three in December-February. Models suggest the ITCZ may shift equatorward in March-May and June-August, although displacement is small.

West Pacific Monsoon: There is a general tendency for an amplification of the seasonal cycle of rainfall in the West Pacific Monsoon region. Westerly winds over the region show a relatively weak enhancement in December-February, while in June-August there are enhanced westerlies in the Northern Hemisphere contrasting with weaker westerlies in the Southern Hemisphere.

Box 6.1: Climate Projection Uncertainties

- Since it is uncertain how society will evolve over this century, it is difficult to know exactly how anthropogenic emissions of greenhouse gases and aerosols will change. Each of the 40 emission scenarios produced by the IPCC is considered plausible, with the range of uncertainty increasing over the 21st century.
- There are subtle differences between models associated with the representation of key physical processes. These important differences result in a range of climate projections for a given emission scenario.
- While climate models are all based on the same physical laws, they are not perfect representations of the real world. Climate models are not equally skilful in simulating the climate of the Pacific. A rigorous evaluation of the ability of the models to simulate the present climate revealed that while most models are able to capture the broad-scale climate features of the region, a number of deficiencies exist, particularly for tropical rainfall. When a country is located in a region with model deficiencies, less confidence can be placed on climate projections.
- Models differ in their estimates of the strength of different feedbacks in the climate system, particularly cloud feedbacks, oceanic heat uptake and carbon cycle feedbacks.
- Direct and indirect aerosol impacts on the magnitude of the temperature response, on clouds and on precipitation remain uncertain.
- Future changes in the Greenland and Antarctic ice sheet mass are a major source of uncertainty that affect sea-level rise projections.
- Confidence in projections is higher for some variables (e.g. temperature) than for others (e.g. precipitation), and it is higher for larger spatial scales and longer averaging periods.
- Some of the most difficult aspects of understanding and projecting changes in regional climate relate to possible changes in the circulation of the atmosphere and oceans, and their patterns of variability.
- Many important small-scale processes cannot be represented explicitly in models, and so must be included in approximate form as they interact with larger-scale features. This is partly due to limitations in computing power, but also results from limitations in scientific understanding or in the availability of detailed observations of some physical processes.
- Downscaling methods have been specifically developed for the study of regional- and local-scale climate change, but these have advantages and disadvantages.
- When interpreting projected changes in the mean climate, it is important to remember that natural climate variability (e.g. the state of the El Niño-Southern Oscillation) will be superimposed and can cause conditions to vary substantially from the long-term mean from one year to the next, and sometimes from one decade to the next.